HHS Public Access

Author manuscript

Nat Neurosci. Author manuscript; available in PMC 2018 October 23.

Published in final edited form as:

Nat Neurosci. 2018 May ; 21(5): 671–682. doi:10.1038/s41593-018-0138-9.

Synaptic nanomodules underlie the organization and plasticity of spine synapses

Martin Hruska[1], **Nathan Henderson**[1], **Sylvain J Le Marchand**[2], **Haani Jafri**[1], and **Matthew B Dalva**[1,*]

[1]Department of Neuroscience, The Vickie and Jack Farber Institute for Neuroscience, Thomas Jefferson University, Philadelphia, PA

Abstract

Experience results in long-lasting changes in dendritic spine size, yet how the molecular architecture of the synapse responds to plasticity remains poorly understood. Here, a combined approach of multi-color stimulated emission depletion microscopy (STED) and confocal imaging demonstrates that structural plasticity is linked to the addition of unitary synaptic nanomodules to spines. Spine synapses *in vivo* and *in vitro* contain discrete and aligned sub-diffraction modules of pre- and post-synaptic proteins whose number scales linearly with spine volume. Live-cell time-lapse super-resolution imaging reveals that N-methyl-D-aspartate receptor (NMDAR)-dependent increases in spine size are accompanied both by enhanced mobility of pre- and post-synaptic modules that remain aligned with each other and by the coordinated addition of new nanomodules. These findings suggest a simplified model for experience-dependent structural plasticity relying on an unexpectedly modular nano-molecular architecture of synaptic proteins.

Introduction

Experience and NMDAR-dependent plasticity induce long-lasting changes in dendritic spine shape and size, which are thought to be a structural correlate of learning and memory[1–3]. Dendritic spines contain specialized structures called post-synaptic densities (PSDs) that are directly apposed to pre-synaptic neurotransmitter release sites and which scale in size with changes in synaptic strength[4,5]. Influx of calcium into dendritic spines following the activation of NMDARs triggers translocation and accumulation of key proteins of the PSD such as the MAGUK, PSD-95 and leads to lasting changes in synaptic strength[6]. Despite having understood this relationship for many years, the molecular dynamics of the translocation and accumulation of PSD proteins following structural plasticity remains poorly understood.

*Correspondence to: Matthew B Dalva, matthew.dalva@jefferson.edu.

[2]Present address: Bio-Imaging Center, University of Delaware, Newark, DE

Author contributions: M.H. designed and conducted experiments, and wrote the paper, N.H. and S.J.L.M. designed and conducted experiments, H.J. conducted experiments, M.B.D designed experiments and wrote the paper.

Competing financial interests statement: The authors declare no competing financial interests.

Among the structural components of the PSD are MAGUK scaffolding proteins, which anchor and organize the signaling complex of excitatory synapses[4,7]. It has been postulated that the expression of plasticity is mediated by the addition of new 'slots' formed by MAGUKs or MAGUK binding partners that are added to the PSD[8, 10–13]. However, more recent dynamic imaging experiments have challenged this view, suggesting that synaptic structures are fluid, forming a network of barriers to the diffusion of synaptic proteins rather than unitary slots[14–17]. These two models suggest that plastic changes to synapse function may result from either the addition of clustered sets of synaptic components or by the accumulation of molecules trapped in networks of protein complexes. To resolve these important issues, a nanoscale understanding of how key components of the PSD such as PSD-95 are organized and respond to plasticity within individual spine synapses is needed.

The sizes of individual spines, PSDs, and pre-synaptic terminals are strongly correlated, suggesting that the coordinated enlargement of PSDs and pre-synaptic active zones might underlie structural plasticity[18,19]. However, in contrast to post-synaptic changes, much less is known about the impact of NMDAR-dependent plasticity on pre-synaptic organization. Live imaging experiments demonstrated a tight temporal relationship between the enlargement of dendritic spines and pre-synaptic boutons[20]. These findings suggest that similar mechanisms or dynamics may function both pre- and post-synaptically. However, the impact of plasticity on the molecular architecture of the pre-synaptic terminal and how these changes might be related to the organization of the post-synaptic terminal are not known.

Here, using a combination of confocal microscopy, two- and three-color STED and two-color live-cell STED, we demonstrate that structural plasticity of dendritic spines is mediated by coordinated increases in the number of precisely aligned modules of pre- and post-synaptic proteins. Spine synapses *in vitro* and brain slices contain discrete, precisely aligned sub-diffraction nanomodules, whose number, not size, scales with spine volume. Chemical LTP results in an NMDAR-dependent increase in the number of nanomodules in spines. In potentiated spines both pre- and post-synaptic nanomodules show enhanced mobility. Remarkably, despite their enhanced mobility, pre- and post-synaptic modules remained precisely registered, moving as an aligned pair. Thus, our findings suggest a simplified model for experience-dependent plasticity where aligned nanomodules of pre- and post-synaptic proteins function as units, or nanoquanta, of synaptic organization.

Results

Spine size correlates to the number of aligned pre- and post-synaptic modules *in vitro*

Dendritic spine synapses respond to synaptic plasticity with changes in the proteins of the PSD[6]. To begin to determine the link between the spine and the molecular architecture at synapses, we visualized the pre- and post-synaptic nano-architecture in individual dendritic spines under basal conditions in mature 21-27 day *in vitro* (DIV) cultured cortical neurons transfected with only tdTomato. Imaging of cell-filling tdTomato-labeled dendrites enabled visualization of dendritic spines at confocal resolution (>250 nm) while simultaneous dual-color STED imaging of endogenous pre-synaptic vesicular glutamate transporter, vGlut1, and endogenous post-synaptic scaffolding MAGUK protein, PSD-95, was used to examine

nano-organization of excitatory synapses using STED-validated fluorescently conjugated secondary antibodies (resolution of 80-100nm; Fig. 1a-k; Fig. S1).

As expected, combined confocal and STED imaging resolved dendritic spines that contained PSD-95 clusters tightly apposed to vGlut1 clusters spaced at a distance of ~100nm (Fig. 1a, b)[4]. The number of apposed vGlut1 and PSD-95 clusters varied among spines. Most spines contained a single synaptic profile with one PSD-95 puncta aligned with one vGlut1 puncta. However, many spines contained more than one pair of PSD-95 and vGlut1 puncta (Fig. 1a-c, f). In control experiments, the deconvolution algorithm used improved the apparent resolution of our STED images (Fig. S2), but did not introduce or remove clusters even after multiple rounds of photobleaching (Fig. S3)[21]. Analysis of non-deconvolved PSD-95 and vGlut1 images gave similar results as analysis of the same set of images after deconvolution, further validating the use of the algorithm (Fig. S4a, d, g). We confirmed that multiple aligned puncta at spines represented discrete clusters using 3× gated STED confocal microscopy that enabled us to acquire super-resolved images in XY (~50 nm) and Z (~200 nm) of PSD-95 and vGlut1 or PSD-95 and the pre-synaptic active zone marker Bassoon (Fig. S5a, b).

To explore the nano-organization of spine synapses in more detail, three-color STED images of either the synaptic vesicle protein, Synaptophysin-1 (SYP-1), or Bassoon together with vGlut1 and PSD-95, were collected from EGFP-filled cortical neurons (Fig. 2 and 3; Leica SP8 3× gated STED, FWHM ~50 nm). At $EGFP^+$ spines SYP-1 and Bassoon were found to co-localize with vGlut1 and were apposed to PSD-95 puncta (Fig. 2a and Fig. 3a). Consistent with our results from imaging the pre-synaptic marker vGlut1, most spines were apposed to a single SYP-1 or Bassoon puncta, while the remainder of spines were contacted by multiple SYP-1 (Fig. 2a, b) and Bassoon puncta (Fig. 3a-d). Thus, we find that many excitatory synapses are composed of multiple aligned pre- and post-synaptic clusters of endogenous synaptic proteins.

Surprisingly, the average size of individual PSD-95, vGlut1, SYP-1 and Bassoon clusters did not vary between single and multi-cluster spines (Fig. 1d, g; Fig. S4e, h; Fig. 2c and Fig. 3e). Thus, as the number of puncta at a spine increases there is a net increase in the overall amount of PSD-95, vGlut1, SYP-1, and Bassoon found at spine synapses, but the average size of each puncta remains constant (Fig. 1e, h; Fig. 2d; Fig. 3f; and Fig. S4f, i). These results suggest that individual PSD-95 and pre-synaptic clusters may represent modular units of synaptic organization. We termed them “nanomodules”.

To test the hypothesis that nanomodules are units of spine organization, we asked how the number of pre- and post-synaptic modules was related to spine size[17]. The number of PSD-95, vGlut1, SYP-1 and Bassoon clusters scaled with spine size, exhibiting a linear relationship with spine head area (Fig. 1i, j; Fig. 2f, g; Fig. S4b, c; Fig. 2h and Fig. 3h). Larger spines contained more PSD-95, vGlut1, SYP-1, and Bassoon with a significant positive correlation between the total area of PSD-95, vGlut1, SYP-1, or Bassoon per spine and spine head area (Fig. S5c-f). However, cumulative probability histograms of PSD-95, vGlut1, SYP-1, or Bassoon nanomodule areas revealed no significant differences in nanomodule size in single and multi-cluster spines (Fig. 2e and Fig. 3g). These findings

suggest that while the number of nanomodules scales with spine size, the size of individual nanomodules does not change.

To test the possibility that the relationship between the number of nanomodules and spine size was due to a random association between larger spines and nanoclusters, we conducted Monte Carlo simulations (Fig. S6 and Fig. S7). Simulated spines were selected for analysis using the same set of inclusion criteria as used for endogenous spines (Fig. S6c). Of the fraction of simulated spines that were associated with PSD-95 (≤ 4%) or vGlut1 (≤19%) greater than 80% contained only single nanomodules, and a significantly lower fraction of simulated spines contained multiple nanomodules than observed in neurons (Fig. 1c, f; Fig. S6g, h; PSD-95, two and three puncta, $p \leq 0.0142$; vGlut1, two puncta, $p \leq 0.0073$, three puncta, $p \leq 0.0001$, t-test). Similar results were obtained for SYP-1 and Bassoon clusters (Fig. S7i, j). These findings suggest that the number of nanomodules in dendritic spines is not random and may involve an active process. In simulated spines that contained nanomodules, the areas of simulated spines and the number of nanomodules showed little correlation (Fig. S6i, j and Fig. S7k-n), and spine size and nanomodule number in simulated spines was significantly less well correlated than in neurons *in vitro* (Fig. 1i, j; Fig. 2f-g and Fig. 3h). These results support a model where nanomodules are units of spine organization, with module number, not size, scaling with spine area.

The observation that spines may contain multiple pre- and post-synaptic elements suggests that individual pre- and post-synaptic modules might function in pairs, similar to what has been observed by electron microscopy (EM) at perforated synapses[22]. Indeed, we found that the number of PSD-95 clusters increased with the number of vGlut1, SYP-1 and Bassoon nanomodules (Fig. 1k; Fig. 2j; Fig. 3i). These findings demonstrate a relationship between pre- and post-synaptic nano-organization and suggest that the number of PSD-95 and pre-synaptic modules found at a single spine may scale with dendritic spine size.

Synaptic architecture exhibits modular organization *in vivo*

To determine whether dendritic spines in the cortex are also composed of pre- and post-synaptic modules, neurons of the somatosensory cortex were labeled at postnatal day 7 (P7) by injecting a lentivirus that transduced only EGFP. At P28-P35 when many mature dendritic spines are present, we perfused the mice, sectioned the brains and cleared the sections using the CUBIC1/2 method to minimize light scattering during imaging[23,24]. 3D super-resolved images were collected with a gated 3× STED Leica confocal system to image EGFP-labeled spines in confocal resolution (>250 nm) and endogenous PSD-95 and vGlut1 clusters in super-resolution (~80 nm in XY and ~ 200 nm in Z; Fig. 4a, b and Video S1).

Spines were selected from primary and secondary dendritic branches of the apical dendritic arbor where experience-dependent plasticity of spine size occurs[25]. 3D reconstruction of non-deconvolved imaged sections demonstrated that, similar to synapses *in vitro*, dendritic spines *in vivo* contained both single and multiple aligned PSD-95 and vGlut1 pairs (Fig. 4b-d and Video S1). Approximately 40% of spines contained a single PSD-95 cluster apposed to a single vGlut1 cluster, while spines with two, three, four and even five aligned PSD-95 and vGlut1 clusters were also observed (Fig 4d-f). Similar results were obtained from brain sections that were not subjected to CUBIC (Fig. S8a, b, e). Interestingly, in brain sections,

we found fewer spines that consisted of a single module of PSD-95 and vGlut1 than seen *in vitro* (~40% vs. ~60%) with a concomitant increase in the proportion of spines that contained two or more modules. To test whether these differences were due simply to higher density of synaptic clusters in the brain we conducted Monte Carlo simulations (Fig. S9). Simulations resulted in significantly more single nanomodule spines and fewer spines containing multiple PSD-95 and vGlut1 nanomodules than found endogenously (Fig. 4a, f; Fig. S8b, e and Fig. S9f). These data suggest that in brain sections nanomodules are precisely associated with spines.

A lower fraction of spines contains single nanomodules in brain sections than *in vitro*, therefore we asked whether the relationship between spine size and module number was still maintained in neurons of the somatosensory cortex. The average size of PSD-95 and vGlut1 nano-clusters *in vivo* was not significantly different between single and multi-cluster spines (Fig. 4g, h; Fig. S8c, f). Moreover, the number of PSD-95 and vGlut1 clusters scaled with spine size (Fig. 4i, j and Fig. S8h, i) with a significantly steeper slope than expected from the Monte Carlo simulation (Fig. S9h, i). Finally, the number of PSD-95 and vGlut1 nanomodules scaled tightly with each other at spines (Fig. 4k). These data indicate that both *in vivo* and *in vitro* spine synapses are composed of aligned pre- and post-synaptic nanomodules whose number scales linearly with spine size.

Structural plasticity results in spines containing multiple aligned pre- and post-synaptic nanomodules

To examine whether coordinated increases in the number of nanomodules might be linked to structural plasticity that underlies increases in dendritic spine size[3], we examined whether the number of endogenous PSD-95 and vGlut1 modules per spine is impacted by NMDAR-dependent chemical LTP (cLTP)[26]. We hypothesized that the increase in PSD-95 levels observed three hours after induction of structural plasticity might be due to the addition of new post-synaptic modules[20]. We induced spine enlargement with glycine treatment (cLTP) in DIV21-25 cortical neurons transfected with only cell-filling tdTomato. This method results in NMDAR-dependent structural plasticity of approximately 40% of dendritic spines[26–28]. To determine which spines exhibit structural plasticity, neurons were imaged using a spinning disk confocal microscope once every six minutes for three hours after the induction of cLTP (Fig. 5a-e, Video S2 and S3). cLTP resulted in sustained enlargement of ~42% of dendritic spines while the remainder of spines were non-responsive, having no lasting changes in size (Fig. 5f). Increases in spine size following glycine treatment were blocked by pre-treatment with 50 μM APV and 10 μM MK-801 and remained unchanged in control (un-stimulated) neurons imaged for three hours (Fig. 5f, Video S2 and S3).

To determine the impact of cLTP on the synaptic nano-architecture, neurons were fixed immediately at the conclusion of live-cell imaging and stained for endogenous PSD-95 and vGlut1. Retrospective analysis of individual live-imaged spines was conducted using STED and confocal imaging (Fig. 5a-e). In control neurons, which were not treated with glycine, the majority of spines (>65%) contained a single PSD-95 module apposed to a single vGlut1 module, while the remaining < 35% of spines had multiple clusters (Fig. 5a, g-j). In contrast,

spines that increased in size after cLTP contained significantly more PSD-95 modules (Fig. 5b, g).

Plasticity may drive correlated changes in pre- and post-synaptic size[20]. Consistent with this idea, enlarged spines also had significantly more pre-synaptic vGlut1 modules (Fig. 5b, h), suggesting that both pre- and post-synaptic nanomodules are impacted by structural plasticity. Potentiated spines had a shift in pre- and post-synaptic module number with respect to control spines such that only ~40% contained single PSD-95 and vGlut1 nanomodules and ~60% of spines contained multiple PSD-95 and vGlut1 modules (Fig. 5i, j). APV and MK-801 pre-treatment prevented the increases in PSD-95 and vGlut1 nanomodule numbers and reduced the proportion of multi-module spines to less than 40% (Fig. 5d, g-j). Thus, the increases in the number of both pre- and post-synaptic nanomodules appear related to structural plasticity induced by cLTP. Consistent with this model, non-responsive spines, which did not increase in size after cLTP, contained significantly fewer PSD-95 and vGlut1 nanomodules than potentiated spines (Fig. 5c, f-j; PSD-95: $p = 0.006$; vGlut1: $p = 0.03$, t-test). Thus, spine enlargement following cLTP leads to the increase in the number of endogenous PSD-95 and vGlut1 nanomodules resulting in a higher proportion of multi-module spines.

Under basal conditions, synaptic nanomodule size did not differ between single and multi-cluster spines (Fig. 1–3). Therefore, we next tested whether PSD-95 and vGlut1 nanomodules have unitary size following cLTP. In potentiated spines, the size of PSD-95 and vGlut1 nanomodules did not differ from control or non-responsive spines (Fig. 5k, l). However, consistent with the well-established role of neuronal activity in the maintenance of synaptic PSD-95[29,30], treatment with APV and MK-801 during the three-hour imaging period significantly reduced the area of PSD-95 but not vGlut1 nanomodules (Fig. 5k, l). Importantly, in spines that underwent structural plasticity neither pre- nor post-synaptic module size changed as spine size increased (Fig. 5m, n). These results suggest that the coordinated increase in modular pre- and post-synaptic protein complexes may underlie NMDAR-dependent structural plasticity.

Pre- and post-synaptic modules exhibit increased dynamics, yet remain aligned during structural plasticity

Post-hoc analysis following cLTP induction does not allow us to rule out the possibility that the spines that became larger already had multiple modules. Therefore, we simultaneously visualized the dynamic remodeling of pre- and post-synaptic nano-architecture during structural plasticity of dendritic spines. We used live-cell STED imaging of DIV 21-25 cortical neurons following cLTP induction for three hours at ~90 nm resolution. Pre- and post-synaptic nanomodules were visualized in living neurons by separately transfecting two groups of cortical neurons in suspension at DIV 0, one group with PSD-95-EGFP and cell-filling tdTomato and the other with Synaptophysin-mTurq2 (SYP-mTurq2), and then mixing the two sets of neurons (Methods). SYP-mTurq2 was chosen as the pre-synaptic marker for these experiments because Synaptophysin is organized into nanomodules (Fig. 2) and has well-characterized fluorescently tagged expression constructs[31–33].

In unstimulated control neurons, the majority of spines contacted by a SYP-mTurq2^{+} axon contained a single PSD-95-EGFP nanomodule apposed to a single SYP-mTurq2 nanomodule (Fig. 6a). The average size of control spines did not change over the course of three hours (Fig. S10a) and the number of PSD-95-EGFP and SYP-mTurq2 modules remained stable on average over this imaging period (Fig. 6e, f). As expected from our previous experiments, glycine treatment resulted in two groups of spines: non-responsive spines that remained unchanged in size, and potentiated spines that exhibited a significant long-lasting increase in size (Fig. 6b, c and Fig. S10a). Similar to control spines, non-responsive spines failed to show changes in the number of pre- or post-synaptic nanomodules over the imaging period (Fig. 6b, e, f). Consistent with the hypothesis that structural plasticity results in an increased number of synaptic nanomodules, three hours after glycine treatment potentiated spines contained significantly more of both PSD-95-EGFP and SYP-mTurq2 nanomodules. This increases were blocked by NMDAR antagonists (Fig. 6c-f). These findings indicate that induction of structural plasticity results in the paired increase of pre- and post-synaptic nanomodules.

Structural changes to spine size occur rapidly during the first 30 minutes after induction of plasticity[6,20]. We next asked when changes to the molecular nano-architecture might occur. In potentiated spines, there was a significant increase in the number of PSD-95-EGFP modules within an hour after glycine treatment that remained significantly higher than control for the remainder of the imaging period (Fig. 6e). These findings are consistent with previous work demonstrating a significant rise in PSD-95 levels 60 minutes after LTP stimulation[20]. During the imaging period the size of individual PSD-95-EGFP clusters within single potentiated spines did not change (Fig. S10b). Pre-synaptic SYP-mTurq2 modules also began to increase in number soon after cLTP, and this increase reached significance within two hours post glycine treatment (Fig. 6f). Increases in PSD-95-EGFP and SYP-mTurq2 module number were not observed in non-responsive glycine-treated spines or control-treated spines and were blocked by NMDAR antagonists (Fig. 6a-f). Similar results were obtained when endogenous PSD-95 was labeled with EGFP-FingR PSD-95 intrabodies[34] (Fig. S11a, b; Video S4). These results indicate that the number of modules begins to increase soon after induction of structural plasticity and that by two hours post induction newly aligned pre- and post-synaptic modules are present in potentiated spines. Importantly, while the increase in average nanomodule number is gradual, the average reflects an increasing proportion of spines with multiple modules, which appear to be added in a unitary fashion. These findings highlight the importance of coordinated re-organization of pre- and post-synaptic nano-architecture.

Induction of structural plasticity results in changes to spine dynamics[3]. Therefore, we next examined whether plasticity might result in changes in the organization of synaptic nanomodules. Under basal conditions both PSD-95-EGFP and SYP-mTurq2 modules were not stationary. In control spines both PSD-95-EGFP^{+} and SYP-mTurq2^{+} modules moved similar distances (~1 μm, Fig. 6a, g, h; Video S5). Remarkably, glycine treatment resulted in a significant increase in the mobility of PSD-95-EGFP and SYP-mTurq2 nanomodules in potentiated spines (Fig. 6c, g, h; Video S5). This increased mobility of synaptic modules is likely functionally important for the structural plasticity of synapses because it was blocked by inhibiting NMDARs and absent in non-responsive spines (Fig. 6b, g, h; Video S5).

Consistent with this model, the mobility of endogenous PSD-95 nanomodules visualized using EGFP-FingR intrabodies was significantly higher in potentiated spines than in control or non-responsive spines (Fig. S11c; Video S4).

Increased mobility of synaptic modules following induction of structural plasticity has been suggested to result in changes to the trans-synaptic complex linking pre- and post-synaptic proteins[16]. In this model, mobility of the synaptic nano-architecture might be due to instability in the synaptic structure. Alternatively, movement of pre- and post-synaptic structures might reflect an ordered process linked to the formation of new synaptic components. If plasticity results in increased synaptic disorder, we would expect that pre- and post-synaptic nanomodules might begin to move independently from one another. To test this, we asked whether plasticity changed the total distance that pre- and post-synaptic modules moved. Rather than reflecting disorganization, the enhanced mobility of PSD-95-EGFP and SYP-mTurq2 appears ordered, with each pair of nanomodules moving together (Fig. 6c; Video S5) and covering similar distances during the imaging period (~1.5 μm, Fig. 6g, h).

To examine how plasticity might impact the nanoscale spatial organization of the synapse, we quantified the relationship between pre- and post-synaptic nanomodules using two metrics: distance between the centroids of pairs of modules (d_x) and the alignment between pairs of modules (θ_x; Fig. 6i, Methods). Despite the significantly higher mobility of PSD-95-EGFP and SYP-mTurq2 in potentiated spines, neither the distance between pairs of modules nor the alignment of modules varied significantly between groups (Fig. 6j, k; Video S5). Blockade of NMDARs resulted in a significantly smaller θ_x between pre- and post-synaptic modules, suggesting that neuronal activity may regulate the alignment of nanomodules. Regardless, examination of the movement of PSD-95-EGFP and SYP-mTurq2 modules revealed that these complexes move around the spine head as an aligned pair. These data suggest a model in which the pre-and post-synaptic nano-architecture participates in structural plasticity as a functional unit that spans the synaptic cleft.

Pre- and post-synaptic nano-architecture is rapidly modified following structural plasticity

Induction of NMDAR-dependent structural plasticity results in rapid changes to spine morphology. To begin to examine when the nanoscale changes in synaptic organization occur after induction of structural plasticity, we performed live-cell STED imaging of cultures transfected as described above every 12.5 minutes for one hour (Fig. 7). These experiments revealed that the number of PSD-95-EGFP nanomodules in potentiated spines began to increase within 12.5 minutes of cLTP induction. By 50 minutes after induction of cLTP, potentiated spines contained significantly more PSD-95-EGFP nanomodules than both the control and non-responsive spines (Fig. 7a-c; Video S6). These results suggest that changes to post-synaptic nano-architecture begin within minutes following the induction of NMDAR-dependent plasticity.

Unlike PSD-95, there was a significant increase in SYP-mTurq2 nanomodules in both potentiated and non-potentiated spines immediately after cLTP induction (Fig. 7d; Video S6). These early structural modifications may reflect short-term changes in pre-synaptic function associated with high-levels of neuronal activity[35]. By 25 minutes after cLTP

induction, numbers of SYP-mTurq2 nanomodules in non-potentiated spines had fallen to control levels while in potentiated spines the number of nanomodules was significantly higher (Fig. 7d). These data suggest that changes in pre-synaptic module number may occur prior to the increase in post-synaptic module number.

The number of pre- and post-synaptic nanomodules increases in spines by one hour after induction of cLTP, but shortly after induction of structural plasticity, PSD-95 is thought to undergo a rapid and transient increase in mobility[36]. To examine events that occur during the first 12.5 minutes after induction of cLTP, we first determined the number of PSD-95-EGFP nanomodules in individual tdTomato$^+$ spines using live-cell STED. Then spines with one or two nanomodules were photobleached and fluorescence recovery of PSD-95-EGFP in photobleached spines (FRAP) was monitored following cLTP[36,37]. At the conclusion of FRAP neurons were again imaged with live-cell STED and nanomodule number determined (Fig. 7e, f).

Before cLTP the recovery of PSD-95-EGFP in bleached spines was similar in all conditions (Fig. 7g, h). Induction of cLTP resulted in a rapid and transient increase in PSD-95-EGFP mobility only in spines that were enlarged (≥10% sustained increase over baseline) after cLTP (Fig. 7f-h; Video S7). These findings are consistent with previously published data for structural plasticity induced by photostimulation[36], and suggest that increases in PSD-95 mobility occur rapidly after induction of structural plasticity, are transient, and are specific to spines undergoing structural changes. Although we were able to measure differences in PSD-95 mobility, as expected from rapid live-cell STED imaging, there were no significant changes in PSD-95-EGFP nanomodule number in unenlarged or enlarged spines at this early time point (Fig. 7f). These results suggest that the transient increase in PSD-95-EGFP mobility occurs prior to the increase in the number of PSD-95-EGFP nanomodules.

Discussion

Competing hypotheses have suggested that the synaptic micro-architecture is composed of either ridged structures trapped in nanodomains that form a trans-synaptic column[16] or amorphous fluid-like structures with rapidly transitioning proteins in a dynamic equilibrium[14]. How these two models might explain the ability of the synapse to undergo long-lasting, activity-dependent structural changes has remained obscure. Here, using STED imaging, we demonstrate that spine synapses *in vitro* and *in vivo* are composed of discrete, aligned pre- and post-synaptic protein nanomodules of uniform size, whose number, not size, scales with the size of dendritic spines. Activity-dependent structural plasticity of individual spines results in long-lasting increases in the number of modules. These findings are reminiscent of previous work in the hippocampus suggesting an all-or-none model of synaptic plasticity[38], recent modeling work[39], and are consistent with the observation that some dendritic spines may contain perforated PSDs[22,40,41]. The nano-organization of pre- and post-synaptic proteins was remarkably similar *in vitro* and in brain slices from cortex suggesting that these are robust features of the synapse. Similar post-synaptic nano-clusters of PSD-95 have been observed in the hippocampus[42]. Together, our data indicate that synaptic architecture is composed of modular pre- and post-synaptic organizational units, and that the increase in the number of these modules underlies structural plasticity.

The tight correlation between the sizes of pre-and post-synaptic structures has led to the suggestion that the modifications of pre- and post-synaptic architecture following plasticity may occur in concert[18,19]. However, at most synapses plasticity is thought to be expressed by post-synaptic structural changes downstream of calcium influx through NMDARs[7,43]. Whether long-lasting changes in pre-synaptic molecular organization are associated with NMDAR-dependent plasticity is less clear. In pyramidal neurons, induction of LTP and spine enlargement appear to result in an increase in the size of the associated pre-synaptic boutons[20], while in the amygdala induction of fear learning may result in increased numbers of boutons[44]. Using live-cell dual-color STED imaging we demonstrate that spine enlargement following cLTP leads to the formation of new aligned nanomodules that undergo coordinated rearrangements pre-and post-synaptically. In this respect, multi-nanomodule spine synapses are unexpectedly similar to the neuromuscular junction, containing sets of pre-synaptic sites paired with post-synaptic proteins, which can be added in response to NMDAR-driven plasticity. Fast time resolved live-cell STED imaging indicates that the changes in the number of SYP-1 nanomodules may precede modification to the post-synaptic PSD-95 nano-architecture. These data suggest that the expression of experience-dependent plasticity is not solely a post-synaptic phenomenon, but rather involves both pre- and post-synaptic mechanisms functioning in concert. It will be interesting to determine whether the mechanisms mediating the coordinated increase in pre- and post-synaptic nanomodule number and movement are the same or different and whether these events are linked to changes in the movement of glutamate receptors or spines[12,13,45–47].

How might new nanomodules be generated rapidly after NMDAR-dependent plasticity? One possibility is that nanomodules are recruited as units from dendrites or axons into potentiated synapses. While attractive, this possibility seems unlikely as PSD-95 appears to move between spines by diffusion[48] and we failed to detect nanomodules of PSD-95 moving into enlarged spines after cLTP. However, due to the limitations of live-cell STED microscopy, new nanomodules could have been rapidly delivered to spines. A second possibility is that new nanomodules could be generated by splitting of existing nanomodules. Consistent with this possibility, analysis of nanomodules *in vitro* and in brain slices indicates that both pre- and post-synaptic modules are limited in size. Results from FRAP experiments suggest that the exchange of PSD-95 within a spine increases before changes in the number of nanomodules occur. In this model increases in protein exchange could lead to increases in nanomodule size, driving the formation of new modules once the size limit is reached. Finally, new nanomodules might be linked to the addition of new anchoring proteins. These might be proteins such as AMPARs or AMPAR associated proteins that are added rapidly to the synapse after the induction of synaptic plasticity or trans-synaptic organizing molecules such as ephrin-B3 that interact directly with PSD-95[6,8,10,11,13,37]. Additional work will be required to determine whether one of these models may explain how the number of nanomodules increases in spines following NMDAR-dependent plasticity.

Increased NMDAR-dependent nanomodule movement is linked to the addition of nanomodules and synaptic plasticity. These rapid changes in the movement of synaptic nanomodules are reminiscent of the increased remodeling of the actin cytoskeleton

following NMDAR activation[6,49,50]. Importantly, although mobile, nanomodules at synapses undergoing NMDAR-dependent plasticity remain in precise alignment suggesting that trans-synaptic interactions are maintained during structural plasticity. Thus, even during plasticity, synaptic function would likely remain intact and the regions of the synapse with the highest likelihood of release would remain in precise register with regions of the highest concentration of glutamate receptors[16]. We propose a simplified model for experience-dependent plasticity where induction of structural plasticity within individual spines is mediated by addition of unitary synaptic nanomodules and that these modules or nanoquanta function as building blocks to enable synaptic plasticity.

Online Methods

Animals

All animal studies were approved by the Institutional Animal Care and Use Committee guidelines at Thomas Jefferson University in accordance with US National Institutes of Health guidelines. Mouse pups for lentiviral transduction experiments were obtained from timed pregnant CD-1 mice purchased from Charles River Laboratories Inc. (Wilmington, MA) and housed (3-5 mice per cage) in Thomas Jefferson University's laboratory animal facility. Long-Evans E17-18 rat embryos from timed pregnant animals purchased from Charles River Laboratories Inc. (Wilmington, MA) were used to make primary cortical neuron cultures (see below).

Primary Cortical Neuron Culture preparation

Dissociated cortical neurons were prepared from embryonic day 17-18 (E17-18) rat cerebral cortex as described previously[37,51,52] and cultured in Neurobasal medium (Life Technologies, Carlsbad, CA) supplemented with B27 (Life Technologies), glutamine (Sigma, St. Louis, MO) and penicillin-streptomycin (Sigma). Neurons were plated on poly-D-lysine (BD Biosciences, San Jose, CA) and laminin (BD Biosciences) coated glass coverslips (12 mm, #1.5; Cat#: 64-0712, Warner Instruments, Camden, CT) or in glass bottom 35mm dishes made with #1.5 German optic cover glass (cat#: GBD00004-200, Cell E&G LLC, Houston, TX). Neurons were plated at 150,000/well in 24-well plates or at 180,000 neurons per 18 mm glass coverslip of a single 35 mm dish for transfection experiments and were maintained in a humidified 37°C incubator with 5% CO_2.

Plasmids and Plasmid construction

The tdTomato expression construct used to visualize neuronal morphology was made using a neuronal specific human Synapsin-1 promoter (kind gift from Dr. Peter Scheiffele, University of Basel, Biozentrum) by replacing EGFP between the BamHI and MscI restriction sites with the tdTomato sequence[37]. For visualization of PSD-95-EGFP puncta and neuronal morphology with tdTomato in live-cell STED experiments we used GATEWAY technology (Invitrogen) to generate a plasmid that simultaneously expresses PSD-95-EGFP under control of the human ubiquitin promoter and tdTomato from the human Synapsin-1 promoter (pFUb_PSD-95/hSYN-1_tdTomato)[37,53]. Endogenous PSD-95 in live-cell STED experiments was visualized using EGFP labeled Fibronectin intrabodies generated with mRNA display (FingR) construct under the pCAGGS promoter element[34].

Synaptophysin-1 was tagged at the N-terminus with mTurqouise2. Briefly, HA-tagged Synaptophysin-1 cDNA (NM_009305; kind gift from Dr. Peter Scheiffele, University of Basel, Biozentrum) was subcloned into the NotI/NheI sites of the pCAGGS vector[54]. The mTurquoise2 cDNA was then cloned in frame into the KpnI/XhoI sites just upstream of the HA site in the HA-Synaptophysin-1 pCAGGS vector to generate a fluorescently tagged molecule (pCAGGS_mTurq2-HA-SYP-1).

Neuronal transfection

To control for levels of protein expression, neurons were transfected at day *in vitro* 0 (DIV0) in suspension as previously described[51] using Lipofectamine 2000 (Life Technologies) and fluorescently tagged proteins were under control of mammalian promoters (described above). Briefly, immediately after dissociation of E17-18 rat cortices, cortical neurons were resuspended in OptiMEM (Life Technologies) at 500,000 neurons/mL. 1 mL of suspension was added to 1 mL of the Lipofectamine 2000 / DNA mixture and the transfection mix was incubated at 37°C for 45 minutes. Neurons were subsequently plated either in 24 well plates or in 35 mm dishes and left to adhere to coverslips for 1.5 hours after which they were washed once in cortical medium (Basal Medium Eagle, Life Technologies) supplemented with 10% heat inactivated fetal bovine serum (cat#: S11150H, Atlanta Biologicals, Flowery Branch, GA) and penicillin/streptomycin (Sigma). Neurons were then maintained in Neurobasal medium supplemented with B27 (Life Technologies) and 1% penicillin/streptomycin (Sigma) for 21-25 days at which point they were used for immunocytochemistry and STED or live-cell imaging experiments. 300,000 neurons were transfected with 300 ng of pENTR3-hSYN-1-tdTomato, 1 μg of pFU-PSD-95-EGFP/hSYN-1-tdTomato plasmid or 600 ng of pCAGGS-mTurq2-HA-SYP-1 plasmids. For visualizing endogenous PSD-95, neurons were transfected with 1 μg of the construct encoding EGFP FingR intrabody (pCAG_PSD-95.FingR-eGRP-CCR5TC was a gift from Don Arnold, Addgene plasmid # 46295) along with 300 ng of pENTR3-hSYN-1-tdTomato in suspension at DIV0. For live-cell STED simultaneous imaging of pre- and post-synaptic clusters, two groups of neurons were transfected separately either with pFU-PSD-95-EGFP/hSYN-1-tdTomato or pCAGGS-mTurq2-HA-SYP-1 plasmids for 45 minutes at 37°C after which they were combined in a 1:1 ratio when plating onto 35 mm glass bottom coverslips.

Immunocytochemistry

For immunocytochemistry, cultured cortical neurons were fixed between DIV21 and DIV25 in 4% paraformaldehyde (PFA)/2% sucrose in PBS for 8 minutes at room temperature. Fixed neurons were washed three times in PBS, then blocked and permeabilized for 2 hours at room temperature in 1% ovalbumin and 0.2% gelatin from cold-water fish in PBS containing 0.01% saponin. Neurons were then stained for 2 hours at room temperature or overnight at 4°C with the indicated primary antibodies, washed three times in PBS and then immunostained with corresponding secondary antibodies for 45 minutes at room temperature. After washing three times in PBS, coverslips were mounted with MOWIOL and used for confocal and STED imaging.

Lentiviral transduction and immunohistochemistry

The EGFP lentivirus used to label neuronal morphology *in vivo* was generated at Penn Vector Core (University of Pennsylvania, Philadelphia) using the pFUGW plasmid that expresses EGFP under control of the human ubiquitin promoter[53]. Postnatal day 7 (P7) CD-1 male and female pups were anesthetized with 5% isoflurane for 5 minutes and then maintained under 1-2% isoflurane anesthesia while performing bilateral stereotaxic injections of the EGFP lentivirus into somatosensory cortex of the brain (~30 minutes). Sparse labeling of cortical neurons was achieved by delivering 0.6 μl of the EGFP lentivirus (9.05×10^{10} infective particles/mL) into each injection site. To allow for the efficient expression of EGFP, mice were sacrificed three to four weeks post-injection. At P28-35 mice were perfused trans-cardially with PBS followed by 4% PFA. Brains were post-fixed overnight in 4% PFA at 4˚C. After washing three times for 10 minutes in PBS brains were sectioned at 300 μm using a VT-1000S Vibratome (Leica). All subsequent steps were carried out with sections free floating. Sections were cleared using the CUBIC1/2 method[23,24]. Briefly, sections were incubated in CUBIC reagent-1 (25% urea (cat# U5378, Sigma), 25% N, N, N', N'-tetrakis (2-hydroxypropyl) ethylenediamine (Sigma, cat#: 122262) and 0.2% Triton-X100) for three days at room temperature and washed with PBS. After CUBIC reagent-1 treatment, blocking was performed overnight at room temperature in a blocking solution of 10% fetal bovine serum (FBS, Atlanta biological), 1% bovine serum albumin (BSA, cat# 10857, Affymetrix, Cleveland, OH) and 0.2% Triton-X100 (cat# T9284, Sigma) diluted in PBS. Sections were incubated with primary antibodies diluted in blocking solution for three days at room temperature, washed three times for 10 minutes with PBS and stained with secondary antibodies diluted in blocking solution for three days at room temperature. The stained samples were then washed with PBS and immersed in CUBIC reagent-2 (50% sucrose (BP220-1, Fisher Scientific), 25% urea, 10% tri-ethanolamine (cat# T58300, Sigma) and 0.1% Triton-X100) overnight at room temperature. The cleared sections were then mounted using CUBIC-2 reagent on slides, covered with #1.5 cover glass and used for STED imaging.

For the experiments in non-cleared brain sections, fixed brains were sectioned at 50 μm. Prior to immunostaining, antigen retrieval was carried out by incubating sections in ddH_2O for 5 minutes at 37˚C followed by 0.2N HCl containing 0.5 mg/ml pepsin protease for 10 minutes at 37˚C. Sections were then blocked overnight at 4˚C in 10% FBS, 1% BSA, and 0.2% Triton-X100 in 1× PBS, incubated overnight at 4˚C with primary antibodies, washed 3 times in PBS, incubated for 2 hours at room temperature with secondary antibodies, washed 3 times in PBS then mounted. Delivery of EGFP by lentivirus was used only to label neuronal morphology. No manipulation of protein expression was performed and, therefore, no randomization was done in animal studies.

Antibodies

All primary and secondary antibodies were profiled in our previous publications and were reported to be specific[37,51,52,55]. Primary antibodies: mouse monoclonal (IgG2A) anti-PSD-95 clone K28/43 (1:1000 (ICC) or 1:200 (IHC), Neuromab, UC Davis, Davis, CA), mouse monoclonal (IgG1) anti-Synaptophysin-1 (1:1000, cat # 101 111, Synaptic Systems, Gottingen, Germany), guinea pig polyclonal anti-vesicular glutamate transporter 1 (α-

vGlut1; 1:5000 (ICC) or 1:2500 (IHC), Milipore, Temecula, CA, cat#: AB5905), guinea pig polyclonal anti-Bassoon (1:300, Synaptic Systems, Gottingen, Germany), rabbit anti-Bassoon (1:300, cat #: 141 003, Synaptic Systems), rabbit anti-RFP (1:500, Rockland, Limerick, PA, cat# 600-401-379), rabbit anti-GFP (1:500, Abcam, Cambridge, MA, cat# ab290). Secondary antibodies: Goat anti mouse IgG2A Atto 425 (1:250, Rockland, Inc., cat# 610-151-041), Goat anti-mouse IgG1 Atto-647N (1:500, cat # 610-156-040, Rockland, Inc.), Goat anti-rabbit Atto-647N (1:500, cat # 611-156-122, Rockland, Inc.), Donkey anti-guinea pig AlexaFluor-488 (1:500, Jackson ImmunoResearch, West Grove, PA, cat# 706-545-148), Donkey anti-rabbit Cy3 (1:500, Jackson ImmunoResearch, cat# 711-165-152), Donkey anti-rabbit AlexaFluor-488 (1:500, Jackson ImmunoResearch, cat# 711-545-152), Donkey anti-mouse AlexaFluor-594 (1:500, Jackson ImmunoResearch, cat# 715-585-150), Donkey anti guinea pig AlexaFluor-594 (1:500, Jackson ImmunoResearch, cat # 706-586-148), Donkey anti-guinea pig AlexaFluor-647 (1:500, Jackson ImmunoResearch, cat# 706-605-148).

Chemical LTP

NMDAR-dependent chemical LTP was induced by treatment of DIV21-25 cortical neurons transfected with tdTomato or pFUG-PSD-95-EGFP/hSYN-1-tdTomato and pCAGGS-mTurq2-HA-SYP-1 with 200 μM glycine as described[26,28]. Neurons were placed in artificial cerebrospinal fluid (ACSF, 143 mM NaCl, 5 mM KCl, 2 mM $CaCl_2$, 1 mM $MgCl_2$, 30 mM Glucose and 10 mM HEPES, pH 7.4) containing 0.5 μM TTX, 1 μM Strychnine and 20 μM Bicuculline. After 15-30 minutes of imaging, cultures of neurons were treated with 10 ml of glycine stimulating solution (143 mM NaCl, 5 mM KCl, 2 mM $CaCl_2$, 0 mM $MgCl_2$, 30 mM Glucose, 10 mM HEPES, pH 7.4, 0.5 μM TTX, 1 μM Strychnine, 20 μM Bicuculline and 200 μM Glycine) for 3-5 minutes, followed by 10 mL of 0 mM $MgCl_2$ containing ACSF. To block cLTP, 50 μM APV and 10 μM of MK-801 were included in the solutions described above. Imaging was then conducted for three hours to monitor long-term changes in spine morphology. Spines were classified as “enlarged” only if their area increased by at least 10% immediately following the application of glycine and remained increased (≥10% over baseline) for the entire imaging period.

Imaging – STED nanoscopy

Dual-color imaging of synaptic structures in fixed and immunostained cultured cortical neurons was conducted on a Leica TCS SP5 STED CW confocal microscope (Leica Microsystems, Mannheim, Germany) containing a 592 nm CW depletion line. Images of fixed neurons were acquired as single optical sections using a resonance scanner (8000 Hz scanning), HyD detectors (set between 100-200%) and 100× oil immersion objective (Leica) with 5-10× zoom to obtain 15-30 nm pixel size. The 442 nm and 488 nm lines were used to excite the Atto-425-labeled PSD-95 and the AlexaFluor-488-labeled vGlut1, respectively. The 592 nm depletion line (at 90-100% power) was used to reduce the point-spread function (PSF) for both fluorophores to ~80 nm. Images were deconvolved using the 80 nm PSF in Leica TCS SP5 software and analyzed in ImageJ (NIH, Bethesda, MD).

For chemical LTP experiments, time-lapse live images were acquired using a confocal spinning disk system equipped with a Yokogawa CSU-10 and Hamamatsu EM-CCD digital camera attached to an inverted Leica microscope and controlled by Volocity software

(Perkin Elmer). Optical sections spaced at 0.3 μm were used to acquire 1-2 μm image stacks of dendrites using a 100× oil immersion objective. Adaptive focus control (Leica) was used to minimize focus shifts during 3-hour image acquisition. After conclusion of live imaging neurons were immediately fixed, stained and subjected to STED imaging. Single optical sections of the same dendritic spines that were imaged live were next imaged with super-resolution (~80 nm) using Leica TCS SP5 STED CW as described above.

Live-cell STED chemical LTP, *in vivo* experiments and three-color STED experiments of cultured cortical neurons were performed using a Leica TCS SP8 gated STED (GSTED) 3× super-resolution system (Leica Microsystems) equipped with a tunable white light laser, CW 592 nm and 660 nm depletion lines and a pulsed 775 nm depletion line. Live-cell STED images of PSD-95-EGFP and mTurquoise2-Synaptophysin-1 and confocal images of cell-filling tdTomato were acquired as stacks (~1μm) with a 100× oil immersion objective using a resonant scanner (8000 Hz) and gated HyD detectors (set at 150-250%). Both EGFP and mTurqoise2 have been shown to undergo effective STED in live-cell experiments[56,57]. Images were maintained in focus during 1-3 hours of imaging using Adaptive Focus Control (AFC, Leica). AFC was set to correct focal drifts at every timepoint and imaging position. For EGFP and mTurquoise2, the 592 nm CW line (at 25-35% power) was used to generate STED. For imaging of fixed brain sections, stacks of images at 100-150 nm intervals were acquired using a 100× oil immersion objective. Maximum XY resolution was adjusted for the individual images to ~ 25 nm/pixel. The 594 nm and 647 nm lines were used to excite the AlexaFluor-594-labeled PSD-95 and the AlexaFluor-647 labeled vGlut1, respectively. The pulsed 775 nm depletion laser was used to generate STED in XY (~70 - 80 nm FWHM) with 10% of the power redirected to the Z donut to generate Z resolution of ~200 nm.

For three-color gated STED images of fixed cultured neurons imaged using Leica SP8 3× GSTED, PSD-95 was labeled with Atto-425, vGlut1 was labeled with Alexa-594 and Synaptophysin1 (SYP-1) or Bassoon were labeled with Atto-647N. Resonance scanning (8000 Hz), gated HyD detectors (set at 100-200%) and 100× oil immersion objective (Leica) with 5-10× zoom to obtain desired pixel size (15-25 nm) was used to acquire stacks at 150 nm image intervals. PSD-95 was excited with the 442 nm line (12-15% power) and the CW 592 nm line (60-65% power) was used to generate STED. Gated HyD detectors adjusted between 0.2/0.3 to 6 nanoseconds were used to acquire vGlut1 (excited with the 594 nm laser at 8-12% maximal power), and SYP-1 or Bassoon (excited with the 647 nm laser at 10-15% maximal laser power). The pulsed 775 nm depletion line (set at 10-15% of maximal laser power) was used to generate STED with a resolution of ~50 nm. For Z depletion, 10% of the 775 depletion line power was re-directed to the Z donut to achieve an image Z-resolved at ~250-300 nm.

Image processing and deconvolution

Raw STED images obtained using SP5 Leica CW STED were subjected either to (1) background subtraction (mean intensity of all pixels in the images) followed by a Gaussian blur (2 pixel size) or (2) deconvolution using SP5 Leica Application Suite Advance Fluorescence Software using 80 nm microscope resolution (determined using 40 nm yellow/green (505/515) beads, cat #: F8795, Thermo Fisher Scientific). Detailed methodology for

each manipulation along with the FWHM are provided in figure S2. Both approaches provided similar results (Fig. 1 vs. Fig. S4).

Raw STED images from sections of CUBIC and non-CUBIC processed brain tissue were processed with only background subtraction followed by 2 pixel Gaussian blur. Images collected using SP8 Leica GSTED from cultured neurons were deconvolved as stacks using Huygens deconvolution software by specifying the point spread function (PSF, Leica SP8/DM6000/100× objective, imaging wavelength), optical sectioning, X, Y and Z pixel resolution[21]. Deconvolution was performed separately for each channel using a maximum of 40 iterations. To validate our deconvolution approach, deconvolved images were compared to images processed with simple background subtraction and 2 pixel Gaussian blur (Fig. S3). The deconvolution algorithm was further tested on extensively photobleached images to examine the effects of deconvolution at low signal-to-noise ratio. Comparison of sequentially bleached images and raw STED images validated our approach (Fig. S3). Image analysis was conducted off-line using Image J.

Image analysis

Super-resolution analysis of PSD-95 and vGlut1 localization in dendritic spines was performed on a per spine basis. Images of spines, acquired at confocal resolution (~250-300 nm) were detected visually and Gaussian blur (2 pixel value) was applied to filter out noise. Individual spines were converted to binary masks by thresholding the resulting tdTomato image. Nanoclusters of labeled PSD-95 and vGlut1 (acquired in STED super-resolution) were identified by binarizing each channel separately using intensity thresholds. Thresholds were defined as the mean + 2 × S.D. of intensity values of a 500×500 image pixel area. Clusters were defined as minimum of 5 and maximum of 200 continuous pixels corresponding to an area of 0.03 – 0.3 μm^2. For three-color STED using gated detectors, clusters were defined as a minimum of 10 and maximum of 100 continuous pixels corresponding to an area of 0.015 – 0.15 μm^2. Separation between individual PSD-95 and vGlut1 clusters was identified from line intensity profiles of nearby clusters in each channel and was defined as the mean + 1.5 × S.D. of a local 50×50 pixel area that approximately corresponded to the average size of a spine head. The resulting thresholded nanomodules were used to determine whether these modules colocalized with individual spines. ROIs of each thresholded spine head were used to manually assign the PSD-95 and vGlut1 puncta to spines. PSD-95 clusters were assigned to a spine if the thresholded pixel areas were entirely within the spine head ROI. vGlut1 clusters were assigned to a spine if the thresholded pixel areas either completely or partially overlapped with the spine head ROI. Based on the size of the synaptic cleft and antibody chains, colocalization was defined as puncta that were separated by no more that 150 nm (Figure 1b). Only spines with clearly identifiable PSD-95 or vGlut1 clusters were included in the analysis.

For analysis of PSD-95 and vGlut1 clusters *in vivo*, outlines of spines were determined in individual z sections of thresholded images. The spine outlines were then overlaid onto the thresholded images of the channels corresponding to PSD-95 and vGlut1 clusters. From these assignments, spine co-localization of each cluster was made independently for each z section. Orthogonal views of the overlaid image stacks were used to verify that individual

clusters co-localized with individual spines in the z plane. Finally, image stacks were overlaid and filtered by an edge-preserving algorithm in Imaris software (Bitplane AG). High-contrast images of puncta within the area that corresponded to the size of the spine head and shaft (approximately 100×100 pixels) were projected in Imaris to generate high-contrast volume rendered images. Volume rendering was performed for each channel separately using a two-voxel separation between thresholded objects. Thresholded clusters that did not colocalize with the area of the spine were discarded. Similar to the *in vitro* cluster analysis, the PSD-95 and vGlut1 channels were binarized separately using intensity thresholds (mean + 2 × S.D. of intensity values within an area of 400×400 pixels). Cluster separation was determined as described above for the *in vitro* cluster analysis. Due to tissue expansion following the CUBIC treatment[58] the separation between aligned pre- and post-synaptic clusters was accepted to be between 100-200 nm by measuring the intensity peaks of aligned clusters. Data for both *in vitro* and *in vivo* spine analysis of module number represent observations and were acquired and analyzed without an experimenter blinding. For the live-cell cLTP and retrospective STED analysis, an experimenter was blinded to the condition and the effect of spine size change by first identifying the cluster numbers and then revealing the change in spine morphology for a given condition.

Analysis of live-cell STED—The 4D (x, y, z, t) deconvolved image stacks acquired from the live-cell STED experiments were aligned using ImageJ macros (Stack reg and Turbo reg) using a rigid body transformation based on the morphology of neuronal dendrites and then were analyzed as maximum intensity projections. Dendritic spines were visualized by applying a Gaussian blur (2 pixel value) to the maximum projections of the tdTomato channel. The presence of PSD-95-EGFP and mTurquoise2-Synaptophysin-1 clusters was assessed for each channel separately in each spine. To identify individual clusters, intensity thresholds were generated using the mean + 2 × S.D. of a local 50×50 pixel area corresponding to the average size of a spine head. The appearance of new clusters was determined visually from time-lapse image series by using the manual tracking algorithm in ImageJ. The identity of new clusters was confirmed from intensity plots by measuring the line profile intensity. New clusters were defined when there was >20% difference between peak intensities of individual clusters and the trough between the peaks of the clusters.

The alignment of pre- and post-synaptic nanomodules in live-cell STED experiments was quantified using two metrics based on two-dimensional projections of the images (Fig. 6i). First, the deviation (θ_x) from perfect alignment (a 90-degree angle, $\theta_x = \theta_i - 90°$) between the centers of PSD-95-EGFP and SYP-mTurq2 modules measured along the long axis of the SYP-mTurq2 centroid was calculated at each time point and summed. This measure reflects the relative apposition of the two modules. Second, the distance (d_x) between the centers of PSD-95-EGFP and SYP-mTurq2 centroids was calculated for each time point. The average angular deviation and centroid distance during the three-hour imaging period were then calculated for each condition. Centroids for SYP-mTurq2 and PSD-95-EGFP were generated using the DrawElipse plugin in ImageJ software (https://imagej.nih.gov/ij/macros/DrawEllipse.txt) by manually tracing each nanomodule at each timepoint.

Monte Carlo simulations

The super-resolved images of PSD-95 and vGlut1 from *in vitro* and *in vivo* experiments were thresholded as described above. For *in vitro* data, thresholded masks for each channel were generated using maximum projection images of the entire z-stack (≤ 1μm). Thresholded images for brain sections were generated from a substack corresponding to the average thickness of a spine (~1 μm). Using thresholded masks, we modeled the probability of overlap between randomly positioned spines of varying areas and actual PSD-95, vGlut1, SYP-1 and Bassoon nanomodule images (Fig. S6, S7 and S9). Spine positions were randomized using the random number generator macro in ImageJ. Clusters were assigned as belonging to simulated spines using the same criteria that were used to manually assign post-synaptic and pre-synaptic nanomodules in our data set – PSD-95 was included only when puncta were entirely within the simulated spine area and pre-synaptic nanomodules were included only when puncta were within or touching the simulated spine (Fig. S6c). Simulations were conducted with a variety of sizes of simulated spines reflecting the variation in spine size observed in our data set (Fig. S6, S7 and S9). Spine area was approximated by a circular area calculated from the average diameter of spines in our raw data set. Monte Carlo simulations were then performed on three randomly selected images from independent experiments. For each channel, simulated spines of a specific size were placed at 500 randomly selected locations overlaid onto each raw image selected using an ImageJ macro. Simulations were conducted in three independent runs for the total of 1500 simulations per spine size. Only simulated spines placed randomly at locations that contacted puncta of synaptic marker proteins were included for further analysis.

Statistical analysis

Data were acquired and analyzed based on the standards in the field, however, no method of randomization was used to determine how samples were allocated to experimental groups and processed. Data are expressed as means ± SEM. All data points collected were included for analysis. Statistical significance of the differences among groups were determined by one-way analysis of variance followed by post-hoc tests as described in individual figure legends, or by two-tailed Student's *t*-test when testing differences between two conditions. Kruskal-Wallis test was used to test differences between cumulative probability distributions as well as the differences between FRAP recovery distributions. P values less than 0.05 were considered statistically significant. For p values less than 0.0001 we are providing a range and not the exact number. See supplementary table 1 for statistical detail. Distribution of the data was assumed to be normal, but this was not formally tested. No statistical methods were used to predetermine sample sizes, but the sample sizes are similar to those reported in previous publications[37,51,52,55]. Group differences in variance were tested for each data set and determined to be similar. Unless stated otherwise, statistical tests were conducted on a per spine basis, from cortical neurons collected from a minimum of three independent transfection experiments/animals (Supplementary Table 1).

Data Availability Statement

All relevant data and analysis are within the paper and its Supporting Information files. Raw image stacks are available upon request to Matthew Dalva (Matthew.Dalva@jefferson.edu).

Supplementary Material

Refer to Web version on PubMed Central for supplementary material.

Acknowledgments

We thank Rachel Hodge and the other members of the Dalva laboratory and Drs. Sandeep Datta and Julie Kauer for helpful suggestions and comments. Grants from NIDA (DA022727), NIMH (MH100093) and the Vickie and Jack Farber Foundation to Dr. Dalva supported this work.

References

1. Feldman DE. Synaptic Mechanisms for Plasticity in Neocortex. Annual review of neuroscience. 2009; 32:33–55. DOI: 10.1146/annurev.neuro.051508.135516
2. Trachtenberg JT, et al. Long-term in vivo imaging of experience-dependent synaptic plasticity in adult cortex. Nature. 2002; 420:788–794. DOI: 10.1038/nature01273 [PubMed: 12490942]
3. Matsuzaki M, Honkura N, Ellis-Davies GCR, Kasai H. Structural basis of long-term potentiation in single dendritic spines. Nature. 2004; 429:761–766. DOI: 10.1038/nature02617 [PubMed: 15190253]
4. Sheng M, Hoogenraad CC. The postsynaptic architecture of excitatory synapses: a more quantitative view. Annual review of biochemistry. 2007; 76:823–847. DOI: 10.1146/annurev.biochem.76.060805.160029
5. Matsuzaki M, Ellis-Davies GCR, Nemoto T. Dendritic spine geometry is critical for AMPA receptor expression in hippocampal CA1 pyramidal neurons. Nature. 2001
6. Bosch M, et al. Structural and Molecular Remodeling of Dendritic Spine Substructures during Long-Term Potentiation. Neuron. 2014; 82:444–459. DOI: 10.1016/j.neuron.2014.03.021 [PubMed: 24742465]
7. Nicoll RA. A Brief History of Long-Term Potentiation. Neuron. 2017; 93:281–290. DOI: 10.1016/j.neuron.2016.12.015 [PubMed: 28103477]
8. Ehrlich I, Malinow R. Postsynaptic density 95 controls AMPA receptor incorporation during long-term potentiation and experience-driven synaptic plasticity. The Journal of neuroscience : the official journal of the Society for Neuroscience. 2004; 24:916–927. DOI: 10.1523/JNEUROSCI.4733-03.2004 [PubMed: 14749436]
9. Migaud M, et al. Enhanced long-term potentiation and impaired learning in mice with mutant postsynaptic density-95 protein. Nature. 1998; 396:433–439. DOI: 10.1038/24790 [PubMed: 9853749]
10. Stein V, House DR, Bredt DS, Nicoll RA. Postsynaptic density-95 mimics and occludes hippocampal long-term potentiation and enhances long-term depression. The Journal of neuroscience : the official journal of the Society for Neuroscience. 2003; 23:5503–5506. [PubMed: 12843250]
11. Bats C, Groc L, Choquet D. The interaction between Stargazin and PSD-95 regulates AMPA receptor surface trafficking. Neuron. 2007; 53:719–734. DOI: 10.1016/j.neuron.2007.01.030 [PubMed: 17329211]
12. Hafner ASS, et al. Lengthening of the Stargazin Cytoplasmic Tail Increases Synaptic Transmission by Promoting Interaction to Deeper Domains of PSD-95. Neuron. 2015; 86:475–489. DOI: 10.1016/j.neuron.2015.03.013 [PubMed: 25843401]
13. Schnell E, et al. Direct interactions between PSD-95 and stargazin control synaptic AMPA receptor number. Proceedings of the National Academy of Sciences of the United States of America. 2002; 99:13902–13907. DOI: 10.1073/pnas.172511199 [PubMed: 12359873]
14. Zeng M, et al. Phase Transition in Postsynaptic Densities Underlies Formation of Synaptic Complexes and Synaptic Plasticity. Cell. 2016; 166:1163–27029504. DOI: 10.1016/j.cell.2016.07.008 [PubMed: 27565345]
15. Blanpied TA, Kerr JM, Ehlers MD. Structural plasticity with preserved topology in the postsynaptic protein network. Proceedings of the National Academy of Sciences of the United

States of America. 2008; 105:12587–12592. DOI: 10.1073/pnas.0711669105 [PubMed: 18723686]

16. Tang AHH, et al. A trans-synaptic nanocolumn aligns neurotransmitter release to receptors. Nature. 2016; 536:210–214. DOI: 10.1038/nature19058 [PubMed: 27462810]
17. Nair D, et al. Super-Resolution Imaging Reveals That AMPA Receptors Inside Synapses Are Dynamically Organized in Nanodomains Regulated by PSD95. The Journal of Neuroscience. 2013; 33:13204–13224. DOI: 10.1523/JNEUROSCI.2381-12.2013 [PubMed: 23926273]
18. Harris KM, Stevens JK. Dendritic spines of CA 1 pyramidal cells in the rat hippocampus: serial electron microscopy with reference to their biophysical characteristics. The Journal of neuroscience : the official journal of the Society for Neuroscience. 1989; 9:2982–2997. [PubMed: 2769375]
19. Schikorski T, Stevens CF. Quantitative ultrastructural analysis of hippocampal excitatory synapses. The Journal of neuroscience : the official journal of the Society for Neuroscience. 1997; 17:5858–5867. [PubMed: 9221783]
20. Meyer D, Bonhoeffer T, Scheuss V. Balance and Stability of Synaptic Structures during Synaptic Plasticity. Neuron. 2014; 82:430–443. DOI: 10.1016/j.neuron.2014.02.031 [PubMed: 24742464]
21. Schoonderwoert V, Dijkstra R, Luckinavicius G. Huygens STED deconvolution increases signal-to-noise and image resolution towards 22nm. Microscopy …. 2013
22. Toni N, Buchs PA, Nikonenko I, Bron CR, Muller D. LTP promotes formation of multiple spine synapses between a single axon terminal and a dendrite. Nature. 1999
23. Susaki EA, et al. Whole-brain imaging with single-cell resolution using chemical cocktails and computational analysis. Cell. 2014; 157:726–739. [PubMed: 24746791]
24. Tainaka K, et al. Whole-body imaging with single-cell resolution by tissue decolorization. Cell. 2014; 159:911–924. DOI: 10.1016/j.cell.2014.10.034 [PubMed: 25417165]
25. Holtmaat A, Svoboda K. Experience-dependent structural synaptic plasticity in the mammalian brain. Nature reviews Neuroscience. 2009; 10:647–658. DOI: 10.1038/nrn2699 [PubMed: 19693029]
26. Lu W, et al. Activation of synaptic NMDA receptors induces membrane insertion of new AMPA receptors and LTP in cultured hippocampal neurons. Neuron. 2001; 29(01):243–254. 00194–5. DOI: 10.1016/S0896-6273 [PubMed: 11182095]
27. Nägerl UV, Willig KI, Hein B, Hell SW, Bonhoeffer T. Live-cell imaging of dendritic spines by STED microscopy. Proceedings of the National Academy of Sciences of the United States of America. 2008; 105:18982–18987. DOI: 10.1073/pnas.0810028105 [PubMed: 19028874]
28. Park M, Penick EC, Edwards JG, Kauer JA, Ehlers MD. Recycling Endosomes Supply AMPA Receptors for LTP. Science. 2004; 305:1972–1975. DOI: 10.1126/science.1102026 [PubMed: 15448273]
29. Sun Q, Turrigiano GG. PSD-95 and PSD-93 play critical but distinct roles in synaptic scaling up and down. The Journal of neuroscience : the official journal of the Society for Neuroscience. 2011; 31:6800–6808. DOI: 10.1523/JNEUROSCI.5616-10.2011 [PubMed: 21543610]
30. Turrigiano GG, Nelson SB. Homeostatic plasticity in the developing nervous system. Nature reviews Neuroscience. 2004; 5:97–107. DOI: 10.1038/nrn1327 [PubMed: 14735113]
31. Li Z, Murthy VN. Visualizing postendocytic traffic of synaptic vesicles at hippocampal synapses. Neuron. 2001; 31:593–605. [PubMed: 11545718]
32. McClelland AC, Sheffler-Collins SI, Kayser MS, Dalva MB. Ephrin-B1 and ephrin-B2 mediate EphB-dependent presynaptic development via syntenin-1. Proceedings of the National Academy of Sciences of the United States of America. 2009; 106:20487–20492. DOI: 10.1073/pnas.0811862106 [PubMed: 19915143]
33. Nakata T, Terada S, Hirokawa N. Visualization of the dynamics of synaptic vesicle and plasma membrane proteins in living axons. The Journal of cell biology. 1998; 140:659–674. [PubMed: 9456325]
34. Gross GG, et al. Recombinant probes for visualizing endogenous synaptic proteins in living neurons. Neuron. 2013; 78:971–985. DOI: 10.1016/j.neuron.2013.04.017 [PubMed: 23791193]
35. Südhof TC. The presynaptic active zone. Neuron. 2012; 75:11–25. DOI: 10.1016/j.neuron.2012.06.012 [PubMed: 22794257]

36. Steiner P, et al. Destabilization of the postsynaptic density by PSD-95 serine 73 phosphorylation inhibits spine growth and synaptic plasticity. Neuron. 2008; 60:788–802. DOI: 10.1016/j.neuron.2008.10.014 [PubMed: 19081375]
37. Hruska M, Henderson NT, Xia NL, Marchand SJ, Dalva MB. Anchoring and synaptic stability of PSD-95 is driven by ephrin-B3. Nature Neuroscience. 2015
38. Petersen CCH, Malenka RC, Nicoll RA, Hopfield JJ. All-or-none potentiation at CA3-CA1 synapses. Proceedings of the National Academy of Sciences. 1998; 95:4732–4737. DOI: 10.1073/pnas.95.8.4732
39. Liu KK, Hagan MF, Lisman JE. Gradation (approx. 10 size states) of synaptic strength by quantal addition of structural modules. Philosophical transactions of the Royal Society of London Series B, Biological sciences. 2017; 372
40. Harris KM, Jensen FE, Tsao B. Three-dimensional structure of dendritic spines and synapses in rat hippocampus (CA1) at postnatal day 15 and adult ages: implications for the maturation of synaptic physiology and long-term potentiation. The Journal of neuroscience : the official journal of the Society for Neuroscience. 1992; 12:2685–2705. [PubMed: 1613552]
41. Sorra KE, Fiala JC, Harris KM. Critical assessment of the involvement of perforations, spinules, and spine branching in hippocampal synapse formation. The Journal of comparative neurology. 1998; 398:225–240. [PubMed: 9700568]
42. Broadhead MJ, et al. PSD95 nanoclusters are postsynaptic building blocks in hippocampus circuits. Scientific reports. 2016; 6
43. Alvarez VA, Sabatini BL. Anatomical and physiological plasticity of dendritic spines. Annual review of neuroscience. 2007; 30:79–97. DOI: 10.1146/annurev.neuro.30.051606.094222
44. Yang Y, et al. Selective synaptic remodeling of amygdalocortical connections associated with fear memory. Nature neuroscience. 2016; 19:1348–1355. DOI: 10.1038/nn.4370 [PubMed: 27595384]
45. Sinnen BL, et al. Optogenetic Control of Synaptic Composition and Function. Neuron. 2017; 93:646–66000000. DOI: 10.1016/j.neuron.2016.12.037 [PubMed: 28132827]
46. Zhang Y, Cudmore RH, Lin DTT, Linden DJ, Huganir RL. Visualization of NMDA receptor-dependent AMPA receptor synaptic plasticity in vivo. Nature neuroscience. 2015; 18:402–407. DOI: 10.1038/nn.3936 [PubMed: 25643295]
47. Huganir RL, Nicoll RA. AMPARs synaptic plasticity: the last 25 years. Neuron. 2013; 80:704–717. DOI: 10.1016/j.neuron.2013.10.025 [PubMed: 24183021]
48. Gray NW, Weimer RM, Bureau I, Svoboda K. Rapid redistribution of synaptic PSD-95 in the neocortex in vivo. PLoS biology. 2006; 4
49. Kim IH, et al. Spine pruning drives antipsychotic-sensitive locomotion via circuit control of striatal dopamine. Nature neuroscience. 2015; 18:883–891. DOI: 10.1038/nn.4015 [PubMed: 25938885]
50. Spence EF, Kanak DJ, Carlson BR, Soderling SH. The Arp 2/3 Complex Is Essential for Distinct Stages of Spine Synapse Maturation, Including Synapse Unsilencing. The Journal of neuroscience : the official journal of the Society for Neuroscience. 2016; 36:9696–9709. DOI: 10.1523/JNEUROSCI.0876-16.2016 [PubMed: 27629719]
51. Kayser MS, McClelland AC, Hughes EG, Dalva MB. Intracellular and trans-synaptic regulation of glutamatergic synaptogenesis by EphB receptors. The Journal of neuroscience : the official journal of the Society for Neuroscience. 2006; 26:12152–12164. DOI: 10.1523/JNEUROSCI.3072-06.2006 [PubMed: 17122040]
52. McClelland AC, Hruska M, Coenen AJ, Henkemeyer M, Dalva MB. Trans-synaptic EphB2-ephrin-B3 interaction regulates excitatory synapse density by inhibition of postsynaptic MAPK signaling. Proceedings of the National Academy of Sciences of the United States of America. 2010; 107:8830–8835. DOI: 10.1073/pnas.0910644107 [PubMed: 20410461]
53. Lois C, Hong EJ, Pease S, Brown EJ, Baltimore D. Germline transmission and tissue-specific expression of transgenes delivered by lentiviral vectors. Science (New York, NY). 2002; 295:868–872. DOI: 10.1126/science.1067081
54. Taniguchi H, et al. Silencing of neuroligin function by postsynaptic neurexins. The Journal of neuroscience : the official journal of the Society for Neuroscience. 2007; 27:2815–2824. DOI: 10.1523/JNEUROSCI.0032-07.2007 [PubMed: 17360903]

55. Nolt MJ, et al. EphB controls NMDA receptor function and synaptic targeting in a subunit-specific manner. The Journal of neuroscience : the official journal of the Society for Neuroscience. 2011; 31:5353–5364. DOI: 10.1523/JNEUROSCI.0282-11.2011 [PubMed: 21471370]

56. Gehne N, et al. Cross-over endocytosis of claudins is mediated by interactions via their extracellular loops. PloS one. 2017; 12

57. Rankin BR, et al. Nanoscopy in a living multicellular organism expressing GFP. Biophysical journal. 2011; 100:5.

58. Richardson DS, Lichtman JW. Clarifying Tissue Clearing. Cell. 2015; 162:246–257. DOI: 10.1016/j.cell.2015.06.067 [PubMed: 26186186]

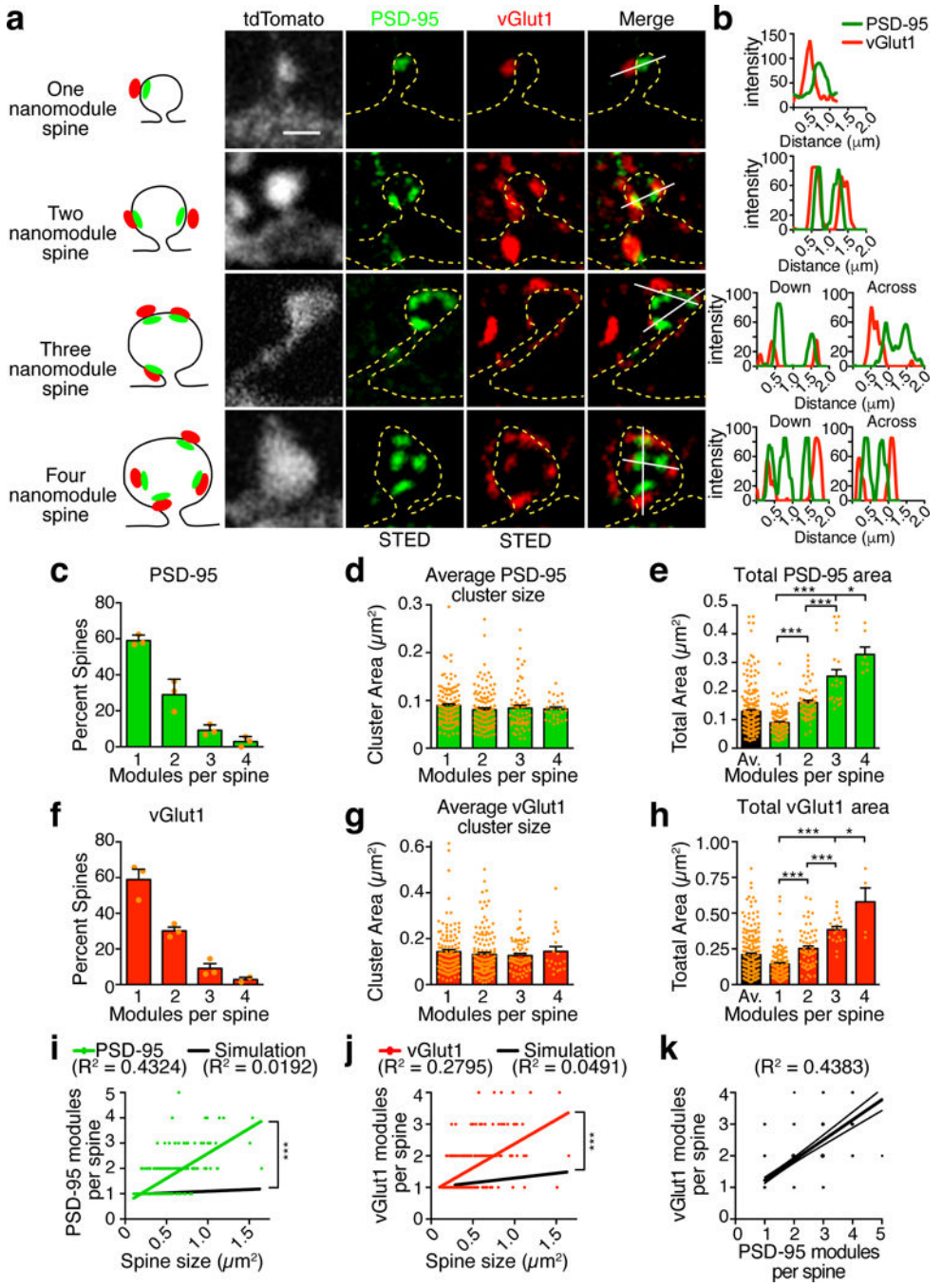

Fig. 1. Modular organization of dendritic spine synapses *in vitro*

(**a**) Representative high-contrast images of PSD-95 (green) and vGlut1 (red) modules imaged with STED (~80 nm FWHM) in dendritic spines imaged simultaneously in confocal mode (~300 nm FWHM, gray and dashed yellow lines) in tdTomato-transfected DIV21 cortical neurons. Scale bar, 0.8 μm. Schematic (left panel) demonstrating the arrangement of multiple synaptic profiles in individual spines from images in the right panel. (**b**) Line profiles (white lines in **a**) of the intensity of PSD-95/vGlut1 labeling in spines from panel **a** indicate a high degree of apposition (~100 nm) of individual pre- and post-synaptic clusters.

(**c and f**) Quantification of the percentage of spines containing single and multiple (**c**) PSD-95 (n = 217 spines) and (**f**) vGlut1 clusters (n = 212 spines, graphs represent mean +/− SEM, dots show percentage of spines from three independent experiments, 9 different neurons). (**d and g**) Quantification of the average areas of individual (**d**) PSD-95, and (**g**) vGlut1 clusters demonstrating no significant size differences between single and multi-cluster spines, one-way ANOVA). (**e and h**) Quantification of the total area of (**e**) PSD-95 and (**h**) vGlut1, one-way ANOVA with Fisher's LSD post-hoc). (**i and j**) Plots of the relationship between cluster number and spine size. Positive correlation of (**i**) PSD-95 (green line, $R^2 = 0.4324$, slope = 1.972 ± 0.1559, $p<0.0001$, F-test, n = 212 spines) and (**j**) vGlut1 (red line, $R^2 = 0.2795$, slope = 1.524 ± 0.1689, $p<0.0001$, F-test, n = 212 spines) cluster number with areas of individual spines (only spines with both PSD-95 and vGlut1 clusters were included for analysis, dots represent cluster number values of individual spines). Monte Carlo simulation (black line) of the relationship between spine size (500 simulations per spine size, spines without PSD-95 and vGlut1 puncta were not included) and the number of (**i**) PSD-95 (simulated slope = 0.1783 ± 0.0355, ANCOVA) and (**j**) vGlut1 (simulated slope = 0.3276 ± 0.0256, ANCOVA) clusters. (**k**) A plot of the relationship between pre- and post-synaptic nanomodules ($R^2 = 0.4383$, slope = 0.6366 ± 0.0497). All experiments were repeated ≥ 3 times. Bar graphs show mean +/− SEM, with numbers of individual spines or clusters represented by dots.

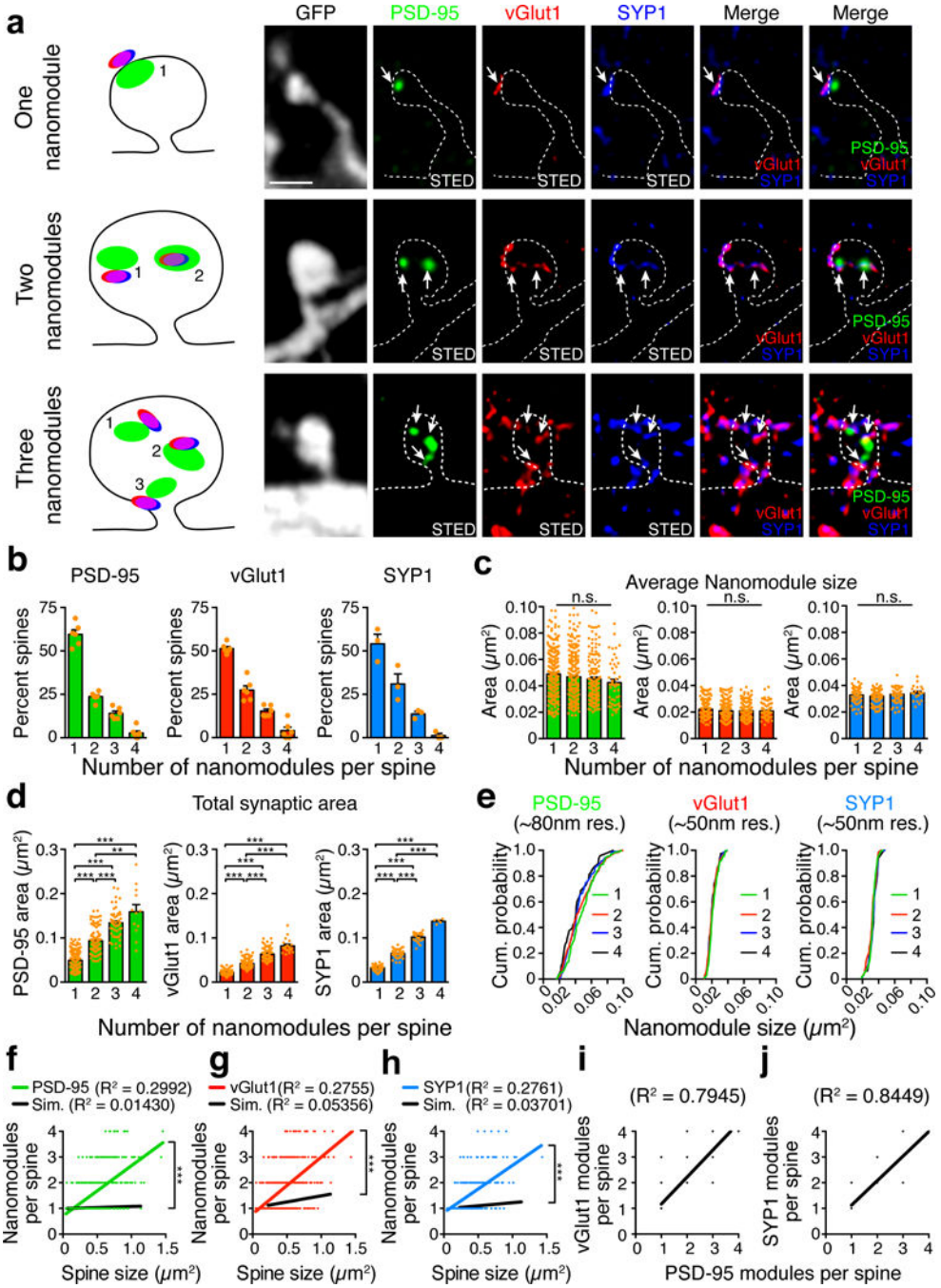

Fig. 2. Synaptic vesicle proteins exhibit modular organization at synapses

(a) Representative high-contrast three-color STED images of PSD-95 nanomodules (green, CW STED, FWHM ~80 nm), vGlut1 (red) and Synaptophysin-1 (SYP-1, blue) nanomodules imaged using gated STED (FWHM ~ 50 nm) in EGFP-labeled dendritic spines of DIV21-25 neurons imaged simultaneously in confocal mode (FWHM ~250 nm, gray and dashed white lines). Scale bar, 1 μm. Schematic (left panel) demonstrating the arrangement of synaptic profiles in individual spines from the images in the right panel. Synaptic profiles were determined as an apposition of co-localized vGlut1 and SYP-1 with PSD-95 (white arrows).

(b) Quantification of the percentage of spines containing single and multiple PSD-95 (n = 406 spines), vGlut1 (n = 406 spines) and SYP-1 nanomodules (n = 189 spines). Data points indicate replicates from ≥ 3 independent transfection experiments. **(c)** Quantification of the average areas of individual PSD-95 (n= 648 clusters), vGlut1 (n= 728 clusters) and SYP-1 nanomodules (n= 310 clusters, one-way ANOVA, Tukey's post hoc). **(d)** Quantification of the total area of PSD-95, vGlut1 and SYP-1 spines; vGlut1; SYP-1, one-way ANOVA, Tukey's post hoc). **(e)** Cumulative probability plots for the data in **c** (Kruskal-Wallis test). **(f-h)** Correlation of spine size with (**f**) PSD-95 nanomodule number (green line, Pearson's R^2 = 0.2992, slope = 1.957 ± 0.1490 (**g**) vGlut1 nanomodule number (red line, Pearson's R^2 = 0.2755, slope = 2.212 ± 0.1785) and **(h)** SYP-1 nanomodule number (blue line, Pearson's R^2 = 0.2761, slope = 1.837 ± 0.2131). Monte Carlo simulation (black line) of the relationship between spine size (spines without PSD-95, vGlut1 and SYP-1 puncta were not included) and the number of (**f**) PSD-95 nanomodules (simulated slope = 0.081 ± 0.02, ANCOVA,), (**g**) vGlut1 nanomodules (simulated slope = 0.474 ± 0.027, ANCOVA) and **(h)** SYP-1 nanomodules (simulated slope = 0.2423 ± 0.019, ANCOVA, SYP-1-containing simulated spines). (**i-j**) A plot of the relationship between PSD-95 nanomodules with **(i)** vGlut1 nanomodules (Pearson's R^2 = 0.7945) and **(j)** SYP-1 nanomodules (Pearson's R^2 = 0.8449). Graphs in **b-d** represent mean +/− SEM, dots show **(b)** percentage of spines, **(c)** individual nanomodules and **(d)** areas from at least three independent experiments, at least 11 different neurons.

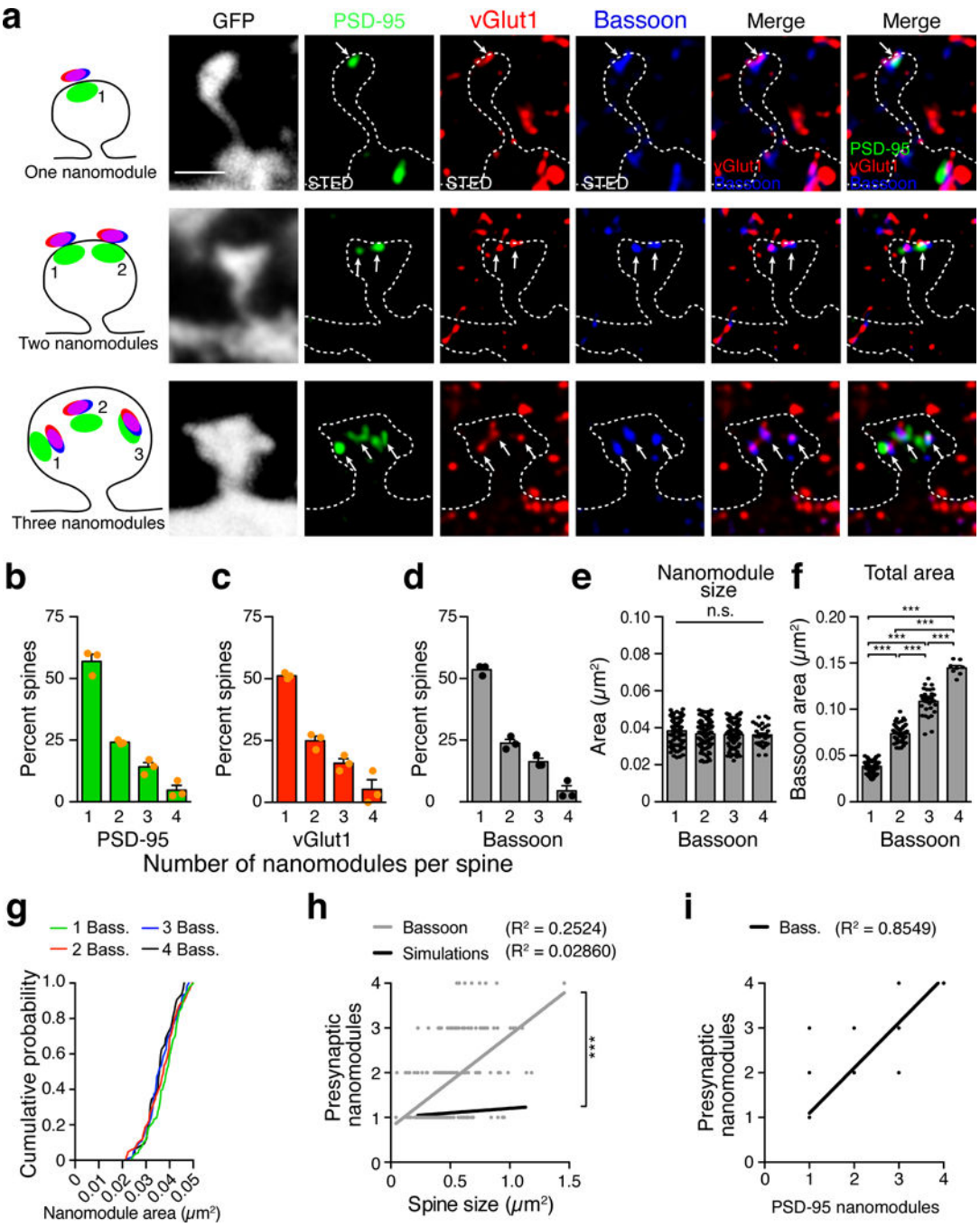

Fig. 3. Synaptic vesicle and active zone markers colocalize at spines as synaptic nanomodules

(a) Representative high-contrast three-color STED images of PSD-95 nanomodules (green, CW STED, FWHM ~80 nm), vGlut1 (red) and Bassoon (blue) nanomodules imaged using gated STED (FWHM ~50 nm) in EGFP-labeled dendritic spines of DIV21-25 neurons imaged simultaneously in confocal mode (FWHM ~250 nm, gray and dashed white lines). Scale bar, 1 μm. Schematic (left panel) demonstrating the arrangement of synaptic profiles in individual spines from the images in the right panel. Synaptic profiles were determined as an apposition of colocalized vGlut1 and Bassoon with PSD-95 (white arrows). Similar results

were obtained from three independent transfection experiments in spines from a total of 10 neurons. **(b-d)** Quantification of the percentage of spines containing single and multiple PSD-95 (n = 217 spines also shown as part of Fig. 2b), vGlut1 (n = 217 spines also shown as part of Fig. 2b) and Bassoon nanomodules (n = 217 spines). Data points represent percent spines with the indicated number of nanomodules in three independent transfection experiments. **(e)** Quantification of the average areas of individual Bassoon nanomodules (n= 379 clusters, one-way ANOVA, Tukey's post hoc). **(f)** Quantification of the total Bassoon area at spines (one-way ANOVA, Tukey's post hoc). Graphs in **b-f** represent mean +/− SEM. **(g)** Cumulative probability plots for the data in **e** (Kruskal-Wallis test). **(h)** Positive correlation of spine size with the number of Bassoon nanomodules (gray line, Pearson's R^2 = 0.2524, slope = 2.065 ± 0.2430). Monte Carlo simulation (black line) of the relationship between spine size and the number of Bassoon nanomodules (spines without Bassoon puncta were not included, simulated slope = 0.2018 ± 0.018, ANCOVA). **(i)** A plot of the relationship between PSD-95 and Bassoon nanomodules (Pearson's R^2 = 0.8549).

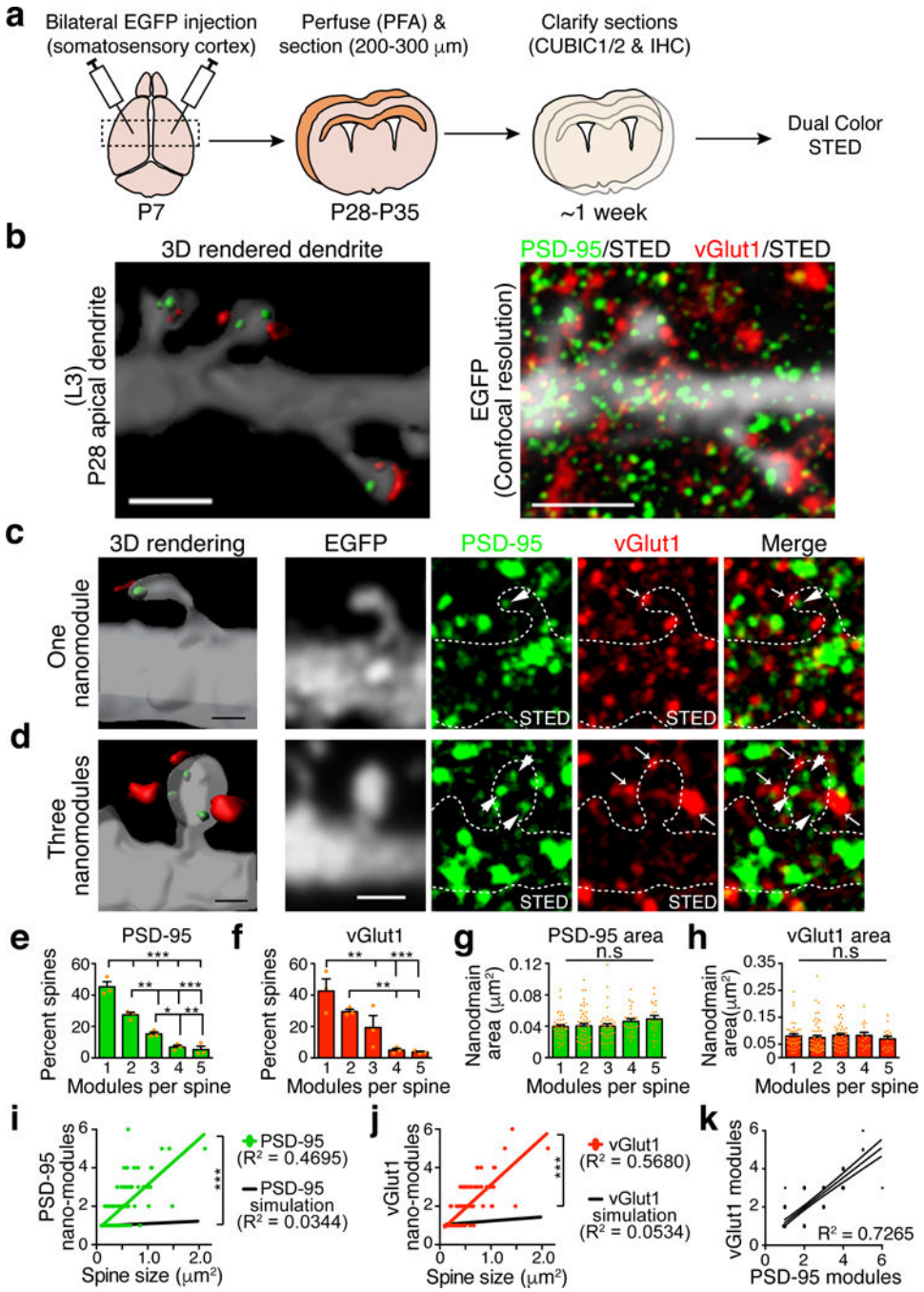

Fig. 4. Modular organization of dendritic spine synapses *in vivo*

(a) Schematic representation of the experiment. (**b**) 3D Imaris reconstruction (left panel) of the dendritic section, spines and corresponding synaptic modules of a layer 3 neuron shown on the right. PSD-95 and vGlut1 puncta not colocalized with spines were removed for clarity. Scale bar, 2 μm. A representative maximum intensity projection image (right panel) from a layer 3 neuron showing an EGFP-labeled apical dendrite (gray) imaged in confocal mode (~300 nm FWHM). Spines were analyzed for PSD-95 (green) and vGlut1 (red) modules by imaging in 3D STED mode (90 nm XY, 200 nm Z FWHM). Scale bar, 2 μm. (**c**)

High-resolution image and corresponding 3D reconstruction of a one-module spine. (**d**) High-resolution image and corresponding 3D reconstruction of a three-module spine. Scale bar, 1 μm for images in **c** and **d**. Spines in 3D rendered images in **c** and **d** were made transparent in order to visualize PSD-95 puncta (green) inside these structures. Scale bars, 0.5 μm. Similar results were obtained from brain sections of three EGFP injected animals. (**e and f**) Quantification of the percentage of spines (n = 3 independent injection experiments) containing single and multiple (**e**) PSD-95 and (**f**) vGlut1 modules (one-way ANOVA, Fisher's LSD post hoc, graphs represent mean +/− SEM, dots show percentage of spines from three independent experiments). (**g and h**) Quantification of the average areas of individual (**g**) PSD-95 (n = 171 clusters) and (**h**) vGlut1 (n = 167 clusters, one-way ANOVA) nanomodules. (**i and j**) Plots of the relationship between cluster number and spine size. A positive correlation of (**i**) PSD-95 (green line, Pearson's $R^2 = 0.4695$) and (**j**) vGlut1 (red line, Pearson's $R^2 = 0.5680$, n = 84 spines, dots represent cluster number values of individual spines) nanomodules numbers with areas of individual spines was observed. Monte Carlo simulation (black line) of the relationship between spine size (500 simulations per spine size, black lines, spines without puncta were removed) and the number of (**i**) PSD-95 (simulated slope = 0.2152 ± 0.0151, measured slope 2.385 ± 0.2766, ANCOVA) and (**j**) vGlut1 (8011 total simulations, simulated slope = 0.5695 ± 0.019, measured slope = 2.427 ± 0.2309,, ANCOVA) clusters. Simulated spines without PSD-95 or vGlut1 clusters were not included in the analysis. (**k**) A plot of the relationship between pre- and post-synaptic nanomodules (Pearson's $R^2 = 0.7265$, n= number of apposed vGlut1/PSD-95 pairs per spine from 84 spines). Bar graphs show mean +/− SEM, with numbers of individual spines or clusters represented by dots.

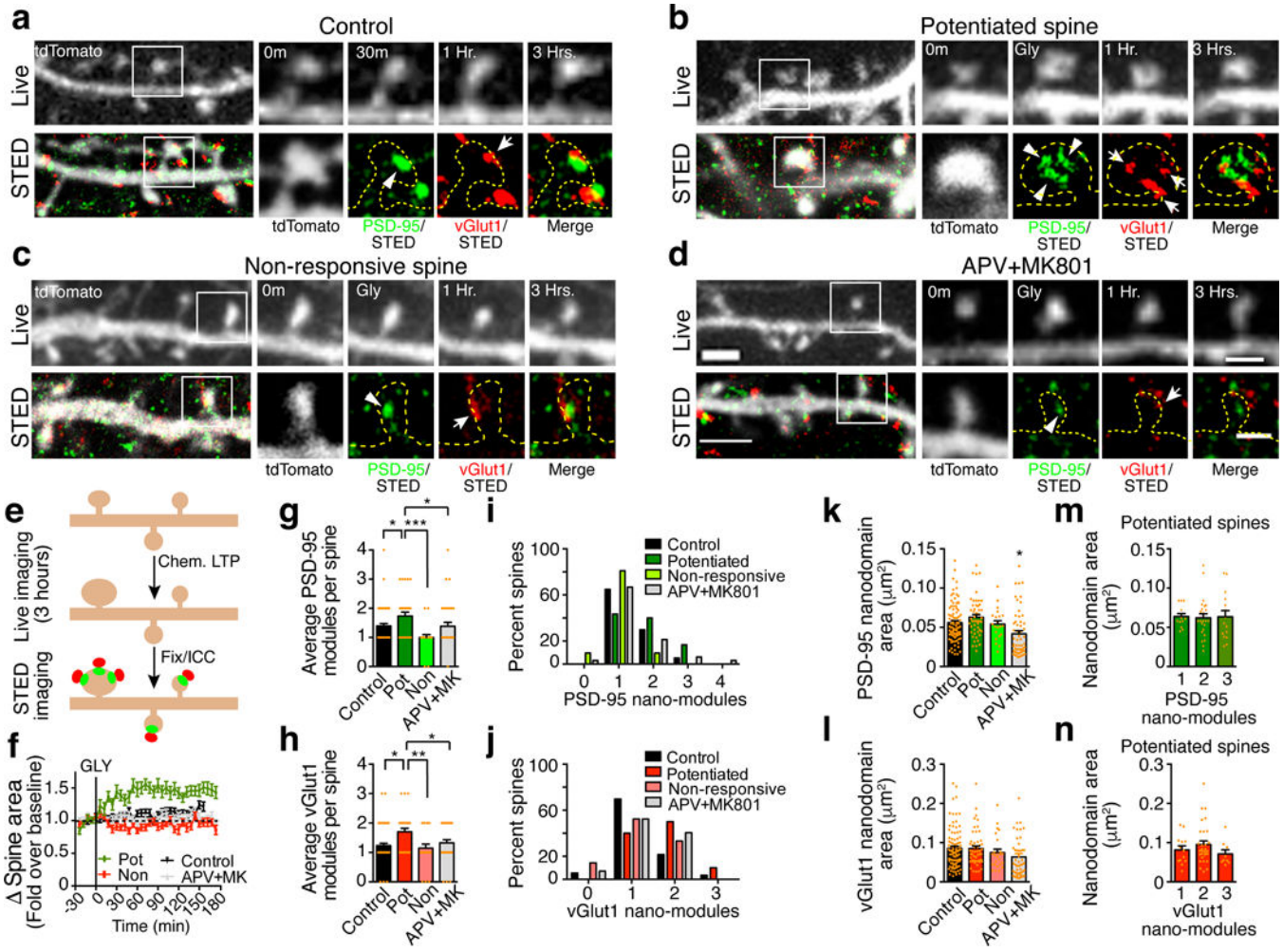

Fig. 5. Structural plasticity associated with cLTP is linked to synaptic module number

(**a-d**) Representative three-hour time-lapse images (top panels, confocal resolution) and retrospective high-contrast STED images (bottom panels) of the same dendritic spines (white squares) of tdTomato-transfected DIV21-25 cortical neurons. Spines (gray and yellow dashed outlines) were imaged at confocal resolution with simultaneous STED imaging of endogenous PSD-95 (green, arrowheads) and vGlut1 (red, arrows). Scale bars corresponding to all images **a-d**: top panel, 2 μm, inset, 1 um; lower panel, 2 μm, inset, 0.75 μm. (**e**) Schematic of the experiment showing initial cLTP live-cell imaging of spine morphology followed by retrospective STED imaging of endogenous proteins at the same spines. (**f**) Quantification of percent change in spine head area during the three-hour live-cell imaging experiment after a three-minute treatment with glycine (200 μM). Potentiated spines were defined by a sustained increase in spine head area of >10% over baseline (green traces, n = 30 spines). Spines that did not increase in size were defined as non-responsive (red traces, n = 21 spines). Spine enlargement was blocked by treatment with the NMDAR blockers 50 μM APV and 10 μM MK-801 (gray traces, n = 34 spines). Control spines were not subjected to glycine treatment (black traces, n = 56 spines). Graph represents mean +/− SEM. (**g and h**) Quantification of the average number of (**g**) PSD-95 and (**h**) vGlut1 module, one-way ANOVA with Fisher's LSD post hoc) in spines from the indicated conditions following

retrospective STED imaging. (**i and j**) Distributions of spines with single and multiple modules in the indicated conditions, binned based on the number of PSD-95 and vGlut1 clusters they contained. (**k and l**) Quantification of the average area of individual PSD- and vGlut1 clusters per spine in the indicated conditions, one-way ANOVA, Fisher's LSD. (**m and n**) Quantification of the average area of individual PSD-95 and vGlut1 modules in single, two and three-module containing potentiated spines (One-way ANOVA). All experiments were repeated ≥ 3 times. Bar graphs show mean +/− SEM, with the numbers of individual spines or clusters represented by dots.

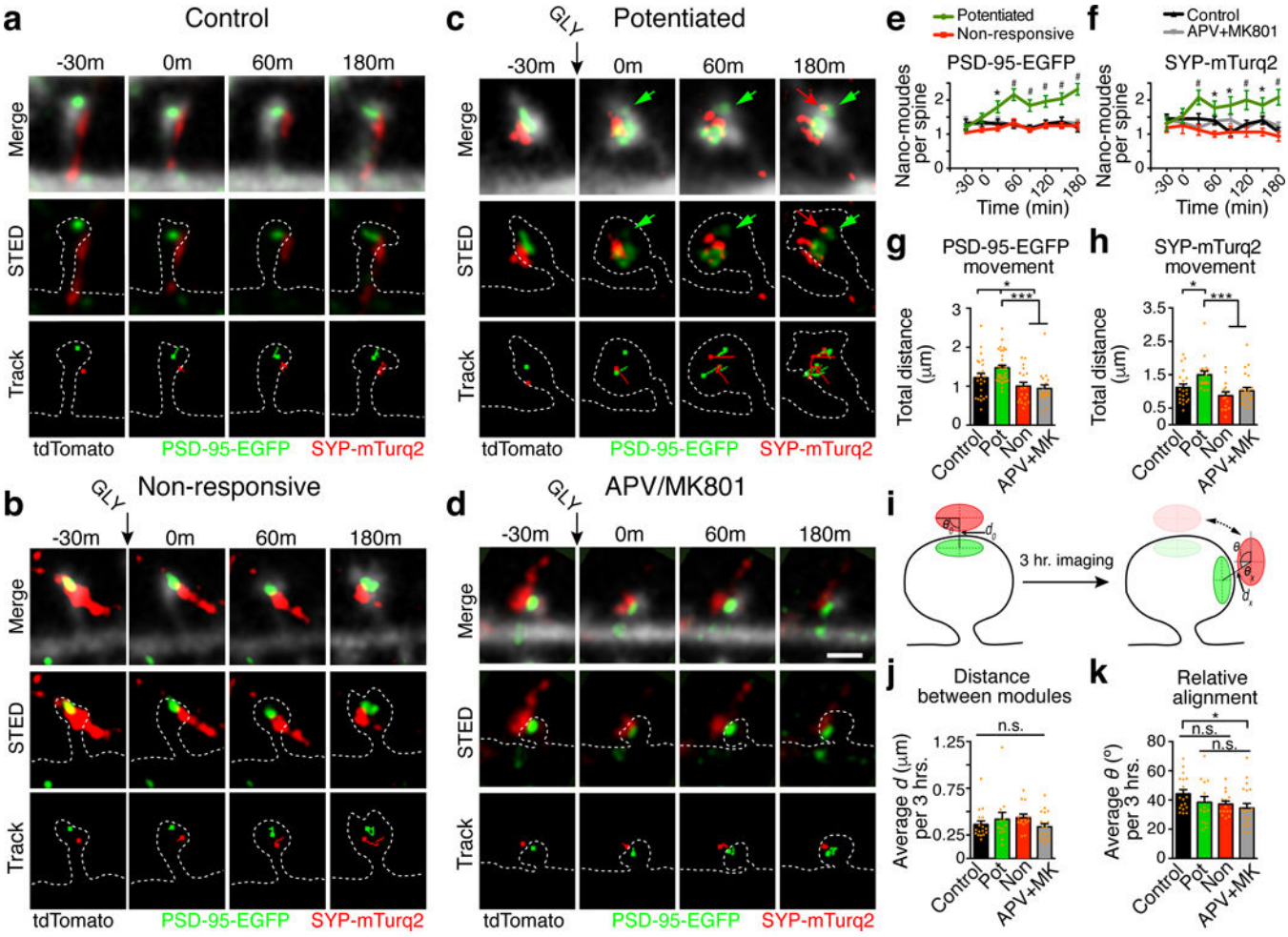

Fig. 6. Rapid remodeling of aligned pre- and post-synaptic modules underlies cLTP structural plasticity

(**a-d**) Representative images of time-lapse dual-color live-cell STED of PSD-95-EGFP (green) and mTurquoise-2-Synaptophysin-1 (SYP-mTurq2, red). Gray shows cell morphology with cell-filling tdTomato in confocal mode. Green and red arrows indicate the appearance of new PSD-95-EGFP and SYP-mTurq2 modules, respectively. Lower 'Track' panels indicate the movement of PSD-95-EGFP (green dots and lines) and SYP-mTurq2 (red dots and lines) modules over the course of imaging (3 hours). Chemical LTP was induced by application of glycine (200 μM, 3 minutes, black arrow). Scale bar corresponding to all images **a-d**, 500 nm. (**e and f**) Quantification of the number of (**e**) PSD-95-EGFP and (**f**) SYP-mTurq2 nanomodules per spine over the course of 3 hours. Measurements were performed at each time point (one-way ANOVA with Fisher's LSD post hoc, "#" = significant differences between all conditions, "*" = significant differences only between Potentiated and Non-responsive conditions). Graphs show mean +/− SEM at each time point). (**g and h**) Quantification of the total distance moved over three hours for (**g**) PSD-95-EGFP (Control, n = 23; Potentiated, n = 34, Non-responsive; n = 19; APV+MK-801, n = 20 modules) and (**h**) SYP-mTurq2 (Control, n = 21; Potentiated, n = 18; Non-responsive, n = 14; APV+MK-801, n = 23 modules; one-way ANOVA with Fisher's LSD post hoc). (**i**)

Schematic representation of the method used to determine the distance and alignment between PSD-95-EGFP and SYP-mTurq2 nanomodules (see Methods). (**j**) Quantification of the average distance between the centers of PSD-95-EGFP and SYP-mTurq2 (Control, n = 18; Potentiated, n = 13; Non-responsive, n = 14; APV+MK-801, n = 20 module pairs, one-way ANOVA). (**k**) Quantification of the relative alignment as described in panel **i** (Control, n = 18; Potentiated, n = 14; Non-responsive, n = 14; APV+MK-801, n = 20 aligned pairs; one-way ANOVA) for the indicated conditions. Treatment with the NMDAR blockers APV +MK-801 resulted in significantly better alignment between PSD-95-EGFP and SYP-mTurq2 (two-tailed Student's t-test). All experiments were repeated ≥ 3 times. Bar graphs represent mean +/− SEM with numbers of individual pre- and post-synaptic clusters **(g and h)** and numbers of aligned pairs of clusters (**j and k**) indicated by dots.

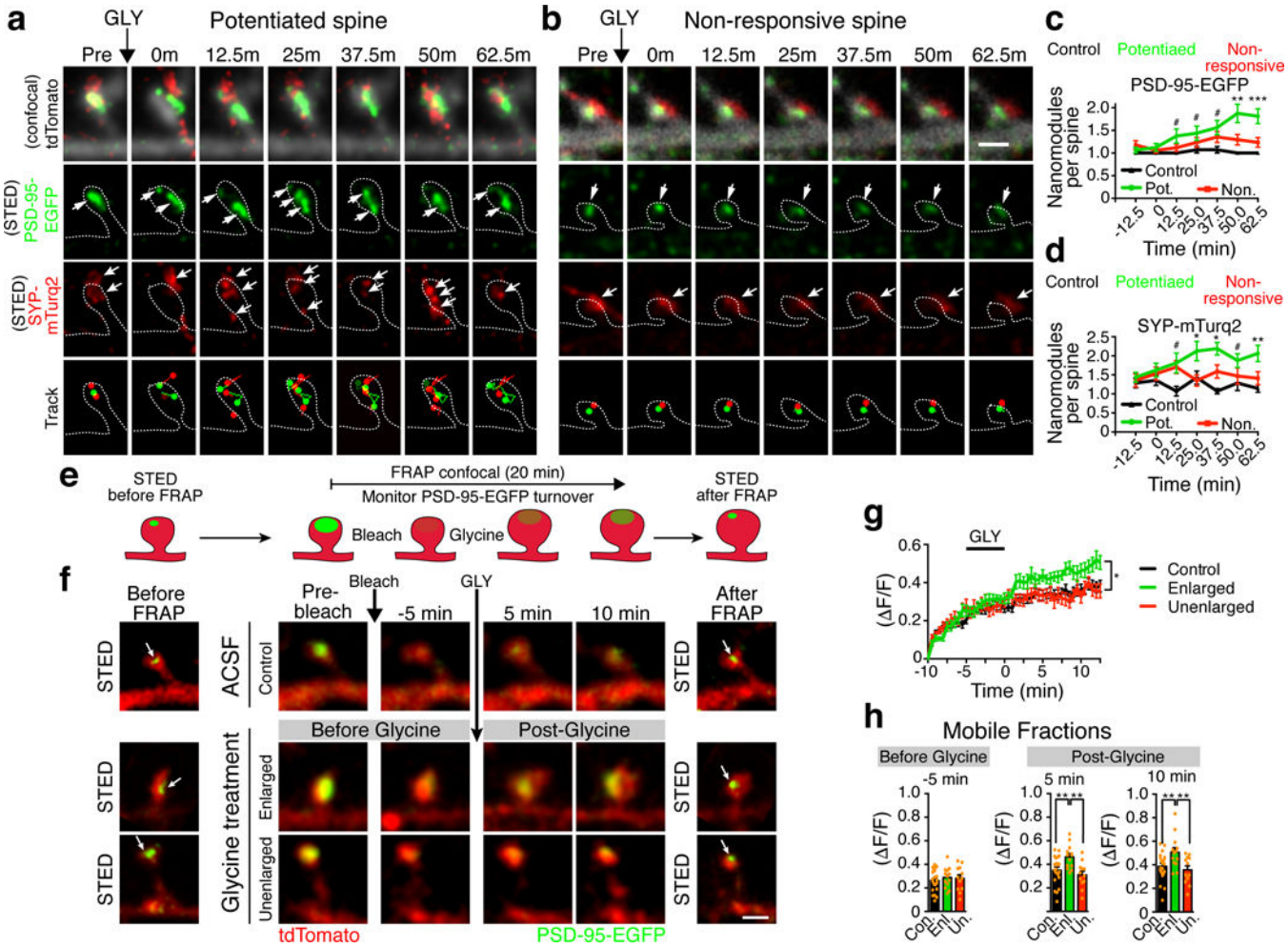

Fig. 7. NMDAR-dependent plasticity is associated with fast modification of synaptic nano-architecture

(a-b) Representative images of time-lapse dual-color live-cell STED of DIV21-25 neurons transfected with PSD-95-EGFP (green) and mTurquoise-2-Synaptophysin-1 (SYP-mTurq2, red). Gray shows cell morphology visualized by cell-filling tdTomato in confocal mode. Lower 'Track' panels indicate the movement of PSD-95-EGFP (green dots and lines) and SYP-mTurq2 (red dots and lines) modules over the course of imaging (1 hour). Arrows indicate the appearance/disappearance of PSD-95-EGFP and SYP-mTurq2 modules during imaging. Chemical LTP was induced by application of glycine (200 μM, 3 minutes, black arrow) and images were acquired every 12.5 minutes for one hour. Scale bar, 1 μm. **(c)** Quantification of the number of PSD-95-EGFP per spine (Control, n = 14; Potentiated, n = 16; Non-responsive, n = 17 spines) over the course of 1 hour. Measurements were performed at each time point (one-way ANOVA with Fisher's LSD post hoc). **(d)** Quantification of the number of SYP-mTurq2 modules per spine (one-way ANOVA with Fisher's LSD post hoc, graphs in **c** and **d** show mean +/− SEM at each time point). **(e)** Schematic for testing the relationship between PSD-95-EGFP nanomodule increase and PSD-95-EGFP turnover immediately following cLTP. **(f)** Representative STED and time-lapse FRAP images of DIV21-25 control, enlarged and unenlarged spines in neurons transfected with cell-filling

tdTomato and PSD-95-EGFP. Scale bars, STED and FRAP images, 1 μm. **(g)** Quantification of PSD-95-EGFP recovery under basal condition and following cLTP. PSD-95-EGFP recovery rapidly increases in enlarged spines following glycine treatment and is significantly higher than in control and unenlarged spines (*p = 0.0119, Kruskal-Wallis, Dunn's post-hoc, Control, n = 21 spines; Potentiated, n = 12 spines; Non-responsive, n =12 spines). **(h)** Quantification of PSD-95-EGFP mobile fractions (calculated from the average of three time points) before glycine (-5 min) and following glycine treatment (one-way ANOVA, Fisher's LSD post hoc, n = number of spines as designated in **g**). Graphs in **h** represent mean +/− SEM. All experiments were repeated ≥ 3 times